Functional analysis and importance for host cell infection of the Ca^{2+}-conducting subunits of the mitochondrial calcium uniporter of *Trypanosoma cruzi*

Miguel A. Chiurillo[a,†,*], Noelia Lander[a,†], Mayara S. Bertolini[a,†], Anibal E. Vercesi[a], and Roberto Docampo[a,b,*]

[a]Departamento de Patologia Clínica, Faculdade de Ciências Médicas, Universidade Estadual de Campinas, Campinas, São Paulo 13083, Brazil; [b]Center for Tropical and Emerging Global Diseases and Department of Cellular Biology, University of Georgia, Athens, GA 30602

ABSTRACT We report here that *Trypanosoma cruzi*, the etiologic agent of Chagas disease, possesses two unique paralogues of the mitochondrial calcium uniporter complex *TcMCU* subunit that we named *TcMCUc* and *TcMCUd*. The predicted structure of the proteins indicates that, as predicted for the *TcMCU* and *TcMCUb* paralogues, they are composed of two helical membrane-spanning domains and contain a WDXXEPXXY motif. Overexpression of each gene led to a significant increase in mitochondrial Ca^{2+} uptake, while knockout (KO) of either *TcMCUc* or *TcMCUd* led to a loss of mitochondrial Ca^{2+} uptake, without affecting the mitochondrial membrane potential. *TcMCUc*-KO and *TcMCUd*-KO epimastigotes exhibited reduced growth rate in low-glucose medium and alterations in their respiratory rate, citrate synthase activity, and AMP/ATP ratio, while trypomastigotes had reduced ability to efficiently infect host cells and replicate intracellularly as amastigotes. By gene complementation of KO cell lines or by a newly developed CRISPR/Cas9-mediated knock-in approach, we also studied the importance of critical amino acid residues of the four paralogues on mitochondrial Ca^{2+} uptake. In conclusion, the results predict a hetero-oligomeric structure for the *T. cruzi* MCU complex, with structural and functional differences, as compared with those in the mammalian complex.

Monitoring Editor
Thomas D. Fox
Cornell University

Received: Mar 14, 2019
Revised: May 6, 2019
Accepted: May 8, 2019

This article was published online ahead of print in MBoC in Press (http://www.molbiolcell.org/cgi/doi/10.1091/mbc.E19-03-0152) on May 15, 2019.

†Present address: Center for Tropical and Emerging Global Diseases and Department of Cellular Biology, University of Georgia, Athens, GA 30602.

*Address correspondence to: Roberto Docampo (rdocampo@uga.edu); Miguel A. Chiurillo (macs@uga.edu).

Abbreviations used: ANOVA, analysis of variance; BAG, buffer A with glucose; BSA, bovine serum albumin; Bsd, blasticidin-S deaminase; CAT, carboxyatractyloside; DAPI, 4,6-diamidino-2-phenylindole; DIC, differential interference contrast; DIG, digitonin; EMRE, essential mitochondrial regulator; FBS, fetal bovine serum; FCCP, carbonyl cyanide *p*-trifluoromethoxyphenylhydrazone; HDR, homologous-directed repair; IFA, immunofluorescence analysis; KO, knockout; LIT, liver infusion tryptose; MCU, mitochondrial calcium uniporter; MICU, mitochondrial calcium uptake; NDK, nucleoside-diphosphate kinase; OCR, oxygen consumption rates; ORF, open reading frames; PAM, protospacer adjacent motif; PBS, phosphate-buffered saline; RFU, relative fluorescence units; RT, room temperature; sgRNA, single guide RNA; TAU, triatome artificial urine; TM, transmembrane domain; VDAC, voltage-dependent anion channel; WT, wild type.

INTRODUCTION

Trypanosoma cruzi is the etiologic agent of Chagas disease or American trypanosomiasis. No vaccines are available against this vector-borne disease, and several challenges remain in the current anti-parasitic drug treatment including partial or lack of activity in the acute or chronic stage of the disease, respectively, and unwanted side effects (Urbina and Docampo, 2003). New therapeutic approaches with novel modes of action are needed against this and other trypanosomiasis.

One of the most promising sources for novel targets is the trypanosome mitochondrion, which is essential for parasite growth and pathogenesis (Menna-Barreto and de Castro, 2014). Several antiparasitic agents target the mitochondria (Vaidya, 2004; Sen and Majumder, 2008; Monzote and Gille, 2010), but these organelles are largely unexplored targets for trypanosomes (Lisvane Silva *et al.*, 2011). One of the mitochondrial pathways that could provide specific targets is the mitochondrial Ca^{2+} transport mechanism, which is functional in the different life cycle stages of *T. cruzi* and is important for their infectivity (Chiurillo *et al.*, 2017; Lander *et al.*, 2018b). In

animal cells this pathway is important for the regulation of mitochondrial metabolism (McCormack *et al.*, 1990), cytoplasmic Ca^{2+} signaling (Carafoli, 2010), and cell death (Kroemer *et al.*, 2007).

T. cruzi has a complex life cycle including replicative and nonreplicative stages in the insect vector (epimastigotes and metacyclic trypomastigotes, respectively) and in its mammalian host (intracellular amastigotes, and cell-derived trypomastigotes, respectively). Although they all possess a functional mitochondrial calcium uniporter (MCU) complex, its role in the regulation of mitochondrial metabolism seems more important in the infective stages (Lander *et al.*, 2018a). Infective stages depend more heavily on an aerobic metabolism of fatty acids and amino acids rather than on glycolysis, as is the case of epimastigotes during the exponential growth phase (Barison *et al.*, 2017; Lander *et al.*, 2018a).

Our finding of the activity of a MCU in *T. cruzi* (Docampo and Vercesi, 1989a,b), together with the finding of its absence in yeast (Carafoli and Lehninger, 1971), were the key (Docampo and Lukes, 2012) to the discovery, first of the modulator mitochondrial calcium uptake 1 (MICU1) (Perocchi *et al.*, 2010) and then of the gene encoding the mammalian pore-forming subunit MCU (Baughman *et al.*, 2011; De Stefani *et al.*, 2011). The MCU complex of animal cells was later shown to include additional components such as the MCU paralogue and dominant negative subunit MCUb (Raffaello *et al.*, 2013), the scaffolding subunit MCU regulator 1 (MCUR1) (Mallilankaraman *et al.*, 2012; Tomar *et al.*, 2016), the essential mitochondrial regulator (EMRE) (Sancak *et al.*, 2013), and MICU2 and MICU3 (Plovanich *et al.*, 2013). We have found that the trypanosome MCU complex differs in composition and function from the mammalian complex. Trypanosomes possess MCU, MCUb, MICU1, and MICU2 orthologues but lack MCUR1, EMRE, and MICU3 (Huang *et al.*, 2013; Docampo *et al.*, 2014). In contrast to what was reported in animal cells (Raffaello *et al.*, 2013), MCUb is not a dominant negative or inhibitory subunit but a Ca^{2+}-conducting protein (Chiurillo *et al.*, 2017; Huang and Docampo, 2018). Trypanosomatids possess, in addition, two extra MCU paralogues that were named MCUc, and MCUd that are also Ca^{2+}-conducting subunits (Huang and Docampo, 2018). These subunits were proposed to form, together with MCU and MCUb, hetero-hexameric complexes in membranes (Huang and Docampo, 2018), in contrast to the in vitro homo-tetramers of recombinant MCU described in fungi (Baradaran *et al.*, 2018; Fan *et al.*, 2018; Nguyen *et al.*, 2018; Yoo *et al.*, 2018), zebrafish (Baradaran *et al.*, 2018), and to the homo-pentamers described in *Caenorhabditis elegans* (Oxenoid *et al.*, 2016).

In summary, the MCU complex is essential for maintaining the bioenergetics of the cell and for determining life–death decisions (Cardenas *et al.*, 2010; Huang *et al.*, 2013). The *T. cruzi* MCU complex has lineage-specific structural and functional differences as compared with the animal complex (Chiurillo *et al.*, 2017; Lander *et al.*, 2018a,b). Selective interference on this pathway in trypanosomes is therefore a valid alternative for drug targeting and its mechanistic study could have important implications for general mitochondrial physiology. In this work, we characterized the calcium-conducting roles of TcMCUc and TcMCUd and analyzed the phenotypic changes that occur in different stages of the parasite upon their overexpression, ablation, or mutagenesis.

RESULTS

MCUc and MCUd homologues in *T. cruzi*

Two genes encoding putative MCUc and MCUd proteins were identified in the *T. cruzi* genomic database (www.tritrypdb.org), *TcMCUc*: TcCLB.506177.110 and *TcMCUd*: TcCLB.511367.330. *TcMCUc* and *TcMCUd* predicted proteins of 235 and 219 amino acids, with an estimated molecular mass of 26.8 and 25.5 kDa, respectively. These newly described MCU complex proteins are conserved only in trypanosomatids and have not been described in other species (Supplemental Figure S1) (Huang and Docampo, 2018). All *TcMCU* paralogues encode proteins with mitochondrial targeting signals (MitoProt II), two transmembrane domains (TM1 and TM2), comparable molecular mass, and sequence similarities in the pore region of TcMCU. It is possible that these paralogues form a hetero-oligomer with TcMCU and TcMCUb, constituting part of the channel, as it was proposed for the *Trypanosoma brucei* orthologues (Huang and Docampo, 2018).

Mitochondrial localization of TcMCUc and TcMCUd and effects of their overexpression

To confirm the mitochondrial localization of TcMCUc and TcMCUd, we overexpressed their HA-tagged versions (*TcMCUc*-OE and *TcMCUd*-OE) in *T. cruzi* epimastigotes. Western blot analyses of epimastigote extracts showed protein bands of 26.9 and 26 kDa, compatible with those of the processed forms (in which the mitochondrial targeting signal has been cleaved) of TcMCUc-3xHA and TcMCUd-3xHA, respectively (Figure 1A). TcMCUc and TcMCUd have a second higher band that could correspond to the unprocessed full-length tagged protein. Mitochondrial localization of both HA-tagged proteins was validated by colocalization with the mitochondrial outer membrane protein voltage-dependent anion channel (VDAC; Figure 1B). *TcMCUc*-OE and *TcMCUd*-OE cells had the same growth rate as control cells transfected with the pTREX-n empty vector (Figure 1C).

To ascertain the capacity of the mitochondria of *TcMCUc*-OE and *TcMCUd*-OE cell lines to take up Ca^{2+}, we monitored changes in fluorescence of Calcium Green-5N in digitonin (DIG)-permeabilized epimastigotes in the presence of succinate as substrate (Figure 1, D and E, H and I). There was a significant increase in mitochondrial Ca^{2+} uptake by either *TcMCUc*-OE or *TcMCUd*-OE epimastigotes, as compared with that of control cells (Figure 1, D and E, H and I). We did not observe modifications in the mitochondrial membrane potential ($\Delta\psi_m$) evaluated by changes in safranine O fluorescence in DIG-permeabilized epimastigotes of *TcMCUc*-OE and *TcMCUd*-OE cells as compared with control cells (Figure 1, F and G, J and K).

Ability of *TcMCUc* and *TcMCUd* knockout (KO) mutants to transport Ca^{2+}

To investigate the ability of *TcMCUc* and *TcMCUd* to transport Ca^{2+}, we generated *null* mutants for these two genes (*TcMCUc*-KO and *TcMCUd*-KO) using the CRISPR/Cas9 method that we adapted to *T. cruzi* (Figure 2, A–H, and Supplemental Figure S2) (Lander *et al.*, 2015, 2018a; Chiurillo *et al.*, 2017; Cruz-Bustos *et al.*, 2018). As described under *Materials and Methods, T. cruzi* epimastigotes were transfected with molecular constructs for the constitutive expression of Cas9 nuclease and single guide RNAs (sgRNAs) to target *TcMCUc* or *TcMCUd* genes (Figure 2, A and E). After selection with blasticidin, we obtained clonal populations from these cell lines by limiting dilution. Using specific sets of primers (Figure 2, B and F; Supplemental Table S1), we confirmed by PCR that both *TcMCUc* and *TcMCUd* genes were ablated and replaced by the DNA donor cassette with the resistance marker at the specific loci (Figure 2, C and G, and Supplemental Figure S2). Southern blot analyses confirmed that *TcMCUc* (Figure 2D) and *TcMCUd* (Figure 2H) were absent in genomic DNA (gDNA) of the KO cell lines.

The ability of mitochondria from DIG-permeabilized *TcMCUc*-KO and *TcMCUd*-KO epimastigotes to take up Ca^{2+} was measured using Calcium green-5N in the presence of 20 μM Ca^{2+} (Figure 2, I–L). Both *TcMCUc*-KO and *TcMCUd*-KO epimastigotes displayed a

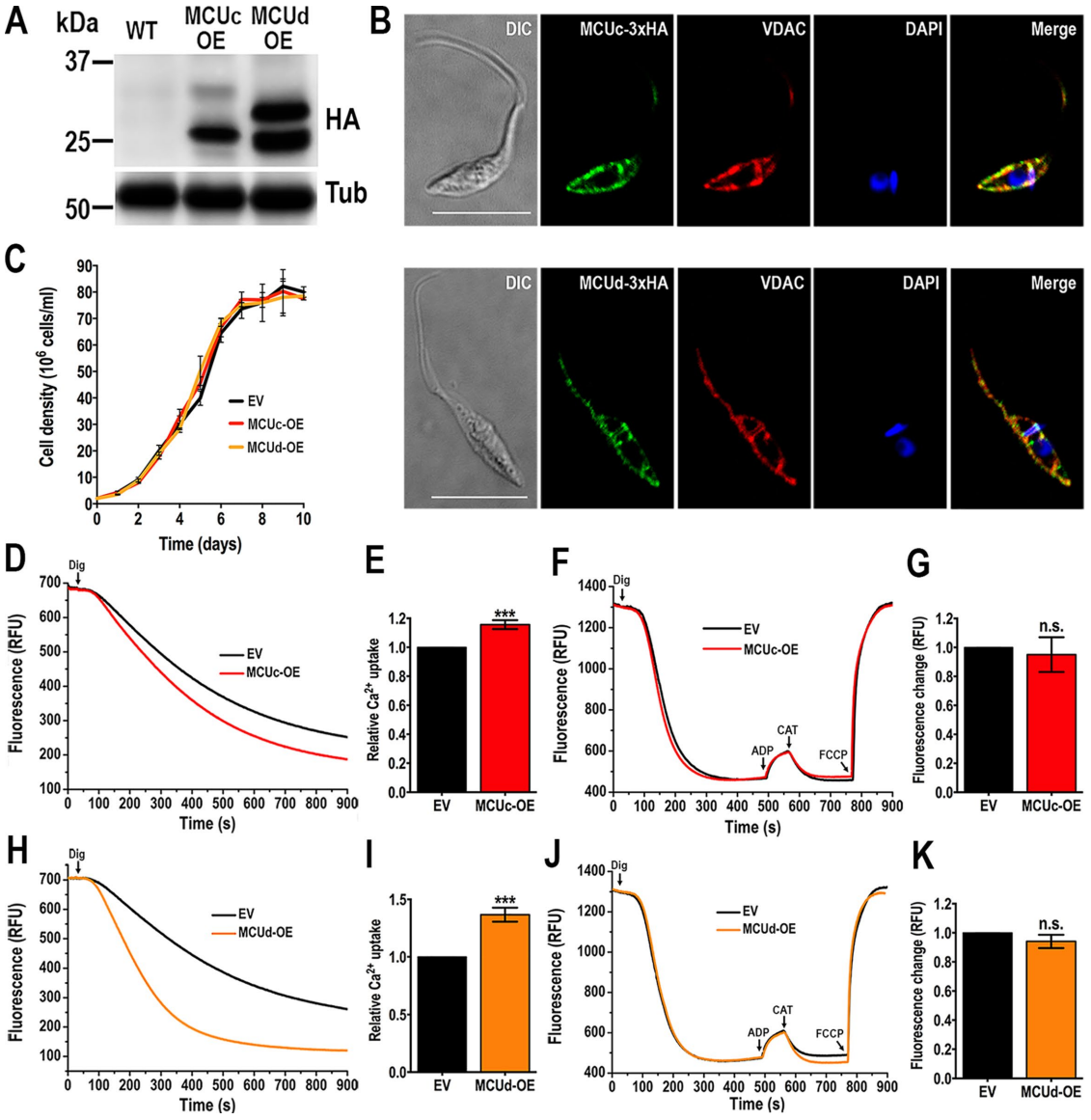

FIGURE 1: Analysis of *TcMCUc* and *TcMCUd* overexpressing cells. (A) *TcMCUc*-3xHA (MCUc-OE) and *TcMCUd*-3xHA (MCUd-OE) overexpression was confirmed by Western blot analysis using anti-HA monoclonal antibodies. WT cells were used as control cell line. α-Tubulin (Tub) was used as loading control. (B) IFA showed colocalization between the green signal of TcMCUc-3xHA (top panel) or TcMCUd-3xHA (bottom panel) and VDAC (red) in the merged image (yellow). DAPI staining (blue) and DIC images are also shown. Scale bars = 10 μm. (C) Growth of control (EV, epimastigotes transfected with pTREXn empty vector), and *TcMCUc* (MCUc-OE) and *TcMCUd* (MCUd-OE) epimastigotes in LIT medium. No significant differences in growth rates were found using one-way ANOVA with multiple comparisons. (D) Representative traces of Ca^{2+} uptake by DIG-permeabilized *TcMCUc*-OE (MCUc-OE) and control (EV) epimastigotes in relative fluorescence units (RFU). The reaction was started after adding 50 μM DIG in the presence of 20 μM free Ca^{2+}, 5 mM succinate and 0.5 μM Calcium Green-5N probe in reaction buffer. (E) Quantification of data from three experiments as shown in D. (F) Changes in mitochondrial membrane potential ($\Delta\Psi m$) of DIG-permeabilized epimastigotes as detected by changes in safranine O fluorescence in EV, control cells, and MCUc-OE, *TcMCUc*-OE cells. Cells (5×10^7) were added to the reaction buffer (2 ml) containing 0.2% BSA, 5 mM succinate, 50 μM EGTA, and 5 μM safranine O. The reaction was started with 50 μM DIG, and 250 μM ADP, 1.5 μM CAT, and 4 μM FCCP were added where indicated. (G) Changes in safranine O fluorescence after addition of ADP to cells used as in F. (H) Representative traces of Ca^{2+} uptake by DIG-permeabilized *TcMCUd*-OE (MCUd-OE) and control (EV) epimastigotes in RFU. The reaction was started after adding 50 μM DIG using the same experimental conditions and additions as D. (I) Quantification of data from three experiments as shown in H. (J) Changes in $\Delta\Psi m$ of DIG-permeabilized epimastigotes as detected by changes in safranine O fluorescence in EV, control cells, and MCUd-OE, *TcMCUd*-OE cells. The reaction was started after adding 50 μM DIG using the same experimental conditions and additions as in F. (K) Changes in safranine O fluorescence after addition of ADP to cells as used in J. In E, G, I, and K, values are means ± SD, $n = 3$; ns, no significant differences; $^{***}P < 0.001$ (Student's *t* test).

negligible capacity for mitochondrial Ca^{2+} uptake (Figure 2, I–L). Similarly to *TcMCUc*-KO, in situ mutated *TcMCUc*^{E162Q} (see below) abolished the mitochondrial Ca^{2+} uptake ability in permeabilized epimastigotes (Figure 2, I and J). Ca^{2+} was taken up by mitochondria of control (scrambled) cells, but not by epimastigotes in which the corresponding gene was ablated. Subsequent dissipation of $\Delta\psi_m$ by carbonyl cyanide *p*-trifluoromethoxyphenylhydrazone (FCCP) caused a rapid increase in fluorescence, indicating mitochondrial Ca^{2+} release (Figure 2, I and K).

To rule out that the defect in mitochondrial Ca^{2+} uptake in the *null* mutant cells was due to mitochondrial membrane depolarization, we evaluated the mitochondrial membrane potential ($\Delta\psi_m$) of DIG-permeabilized epimastigotes in the presence of succinate as mitochondrial substrate and using safranine O. Knockout of either *TcMCUc* or *TcMCUd* did not affect the $\Delta\psi_m$ (Figure 3, A–D). In conclusion, ablation of *TcMCUc* or *TcMCUd* results in a diminished ability of mitochondria to take up Ca^{2+} without affecting their $\Delta\psi_m$.

Phenotypic changes in *TcMCUc* and *TcMCUd null* mutants

TcMCUc-KO, *TcMCUc*^{E162Q} (see below), and *TcMCUd*-KO epimastigotes exhibited similar growth rates in a rich medium liver infusion tryptose (LIT) (Figure 4, A and B). However, the number of cells was significantly reduced in the stationary phase when *TcMCUc*-KO and *TcMCUd*-KO epimastigotes were grown in low-glucose LIT medium (Figure 4C), suggesting that under these growth conditions, a marked decrease in mitochondrial Ca^{2+} uptake affected the bioenergetic functions of this organelle.

To induce the differentiation of *TcMCUc*-KO and *TcMCUd*-KO epimastigotes into infective metacyclic trypomastigotes (metacyclogenesis), we incubated these cells in TAU medium as described under *Materials and Methods*. These cells were able to differentiate to metacyclic trypomastigotes without difference as compared with control cells (transfected with a scrambled sgRNA) (Figure 4D). However, the ability of trypomastigotes to infect tissue-cultured cells (Figure 4B), as well as the replication of intracellular amastigotes (Figure 4F), were significantly impaired in these parasites.

We also evaluated oxygen consumption rates (OCR) under ADP-stimulated (state 3), oligomycin-inhibited (state 4), and FCCP-stimulated (state 3u, uncoupled) conditions in control (scrambled), *TcMCUc*-KO, and *TcMCUd*-KO DIG-permeabilized cells in the presence of succinate as respiratory substrate. Control, *TcMCUc*-KO and *TcMCUd*-KO mitochondria showed well-coupled respiration, although OCR in the presence of ADP, oligomycin, and FCCP were significantly lower in *TcMCUc*-KO and *TcMCUd*-KO mitochondria (Figure 5A). The lower OCR of *TcMCUc*-KO and *TcMCUd*-KO mitochondria correlated with lower citrate synthase activity (Figure 5B), suggesting a mitochondrial defect in these cells.

We analyzed the effect of *TcMCUc* and *TcMCUd* ablations on cell bioenergetics by measuring the adenine nucleotide levels of KO and control parasites under normal culture (incubation in LIT medium) and starvation conditions (incubation in phosphate-buffered saline [PBS]), as described previously (Chiurillo *et al.*, 2017). The results indicate that AMP/ATP ratio is significantly increased under starvation conditions in *TcMCUc*-KO and *TcMCUd*-KO parasites, as compared with control epimastigotes (Figure 5C). However, this result was not correlated with the number of autophagosomes per cell observed in KO parasites under starvation (PBS), as detected by immunofluorescence microscopy using antibodies against ATG8.1 (Figure 5D). ATG8.1 is a marker of autophagosomes that has been used previously to evaluate autophagy in *T. cruzi* (Alvarez *et al.*, 2008). We did not observe differences in the percentage of autophagosomes per cell between *TcMCUc*-KO or *TcMCUd*-KO and control cells.

Microscopy counts of cell viability after treatment with H_2O_2 or C2-ceramide showed that *TcMCUc*-KO and *TcMCUd*-KO epimastigotes exhibited a significant increased ability to resist oxidative stress (225 μM H_2O_2) (Figure 5E) and the effect of proapoptotic agents, such as C2-ceramide (Figure 5F).

Analysis of conserved amino acid residues in the selectivity filter of predicted MCU paralogues

Recent Cryo-EM studies of the recombinant MCU from fungi (Baradaran *et al.*, 2018; Fan *et al.*, 2018; Nguyen *et al.*, 2018; Yoo *et al.*, 2018) and zebrafish (Baradaran *et al.*, 2018) have revealed the formation of homo-tetramers where each of the monomers contribute to the formation of two rings of acidic residues in the selectivity filter. One ring is of larger diameter with each subunit contributing with an aspartate (D), and the second is narrow with each subunit contributing a glutamate (E), analogous to the high-affinity Ca^{2+} site formed by the EEEE locus of Ca_V channels (Nguyen *et al.*, 2018). Taking into account that the MCU channel in trypanosomes is a hetero-oligomer and that each subunit is essential for mitochondrial Ca^{2+} uptake, we aimed at studying whether substitution of critical D and E residues in the WDXXEPXXY domain of each subunit could affect mitochondrial Ca^{2+} uptake. We included in this analysis a D residue which is located N-terminal to the WDXXEPXXY domain and is conserved in three (MCU, MCUc, and MCUd) of the MCU paralogues but not in human MCU (Supplemental Figure S3).

Mitochondrial Ca^{2+} transport is impaired in permeabilized *TcMCU*-KO epimastigotes. However, we were able to reconstitute Ca^{2+} transport in these cells by expressing an exogenous copy of *TcMCU* (Chiurillo *et al.*, 2017) (Figure 6A). We also introduced mutations in the exogenous gene in highly conserved residues to evaluate their ability to restore Ca^{2+} transport in *TcMCU*-KO cells. Western blot analysis confirmed the expression of these proteins (Figure 6A). Complementation with *TcMCU*^{D221N} or *TcMCU*^{D223N} mutants, but not with the *TcMCU*^{E226Q} mutant, was able to partially restore mitochondrial Ca^{2+} uptake (Figure 6, B and C). However, the ability to restore mitochondrial Ca^{2+} uptake by *TcMCU*^{D221N} was greater than that of *TcMCU*^{D223N} (Figure 6C). The results suggest that the glutamate 226 (E226) at the narrow selectivity filter of TcMCU is essential for Ca^{2+} transport, whereas D223 and D221 are important but not essential.

TcMCUb-KO cells exhibit a significantly reduced growth rate (Chiurillo *et al.*, 2017), and all attempts to restore mitochondrial Ca^{2+} uptake by gene complementation of *TcMCUb*-KO cells were unsuccessful. Therefore, we generated in situ *TcMCUb*-WDXXEPXXY mutants by using a CRISPR/Cas9 strategy (Supplemental Figures S4, A and B, and S5, A and B) to introduce mutations in D (D161) and E (E164) residues of this motif (Supplemental Figure S3). Western blot analysis confirmed the expression of these mutated proteins (Figure 6D). In situ mutations in *TcMCUb*^{D161N} resulted in a significant reduction of Ca^{2+} uptake, whereas the *TcMCUb*^{E164Q} substitution abolished the mitochondrial ability to take up Ca^{2+}, similarly to *TcMCUb*-KO epimastigotes (Figure 6, E and F).

TcMCUc and TcMCUd share the same amino acid sequence for the selectivity filter: WNLVEPMTY. Both proteins lack the D residue of WDXXEPXXY motif and, like TcMCU, show an aspartate residue before it (Supplemental Figure S3). We then investigated whether introducing mutations in D and E residues of the putative DWNLVEPMTY selectivity filter of exogenous *TcMCUc* and *TcMCUd* genes could affect their ability to rescue mitochondrial Ca^{2+} uptake in *TcMCUc*-KO and *TcMCUd*-KO cells. We also introduced a mutation in E162 residue of *TcMCUc* by the same knock-in strategy as that used for TcMCUb (Supplemental Figure S5, C and E). Western blot

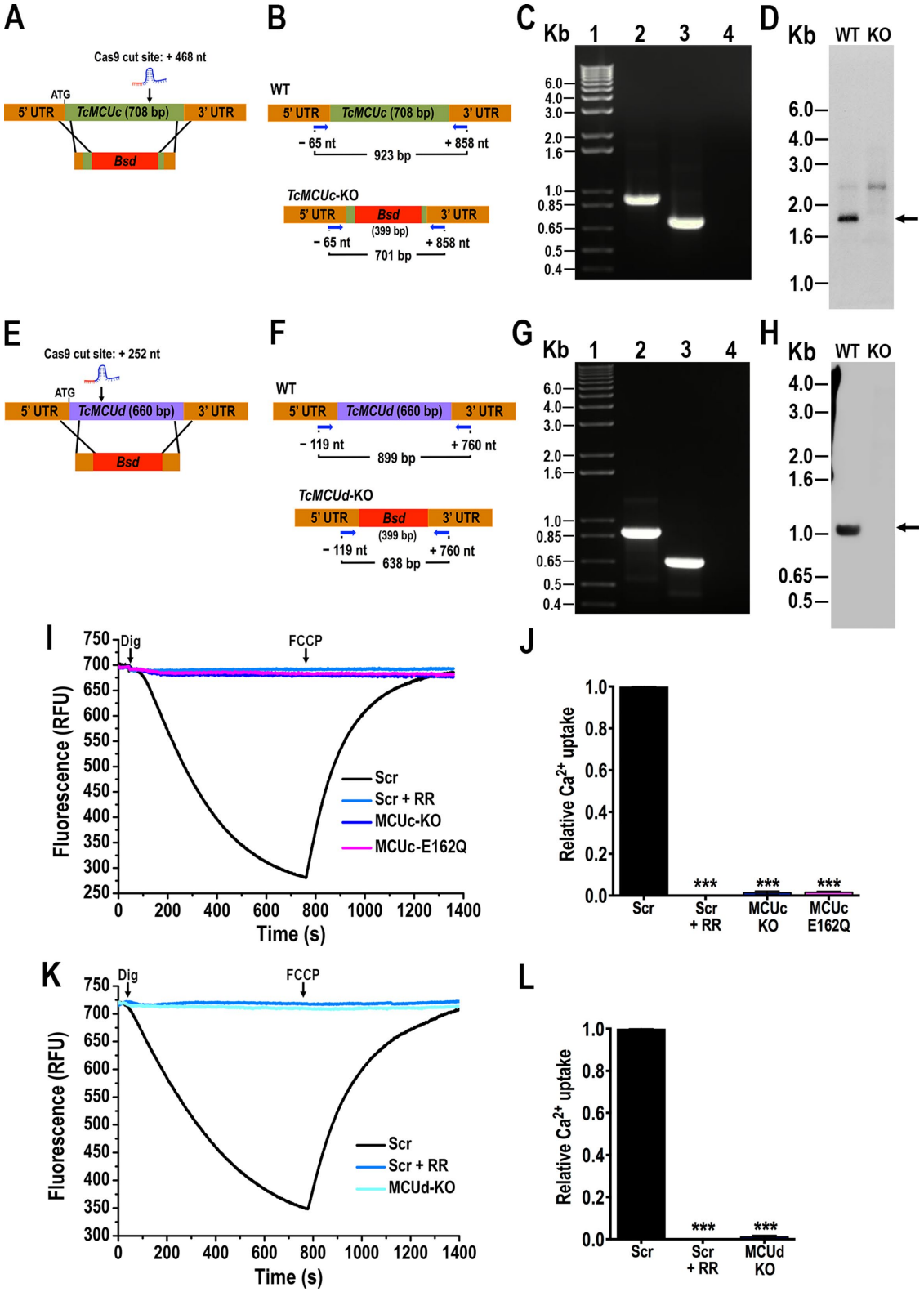

FIGURE 2: Ca^{2+} uptake by *TcMCUc* and *TcMCUd* KOs. (A) Schematic representation of the strategy used to generate a *TcMCUc*-KO mutant by CRISPR/Cas9-induced homologous recombination. A double-stranded gDNA break was produced by Cas9 at nt +468 of the *TcMCUc* ORF (708 base pairs). DNA was repaired with a *Bsd* cassette containing 100–base pair homologous regions spanning from nt –44 to +56 and from nt +677 to +776 of the *TcMCUc* locus. (B) Primers (*arrows*) that were used to verify gene disruption by PCR. The intact locus generates a PCR product of 923 base pairs, while the disrupted locus generates a fragment of 701 base pairs. (C) *TcMCUc* was disrupted at its genomic locus in the KO cell line. Lanes: 1, 1-kb plus ladder; 2, WT; 3, *TcMCUc*-KO mutant cell line; 4, PCR negative control. (D) Southern blot analysis of WT and *TcMCUc*-KO (KO) epimastigotes. The blot was hybridized with a 409–base pair

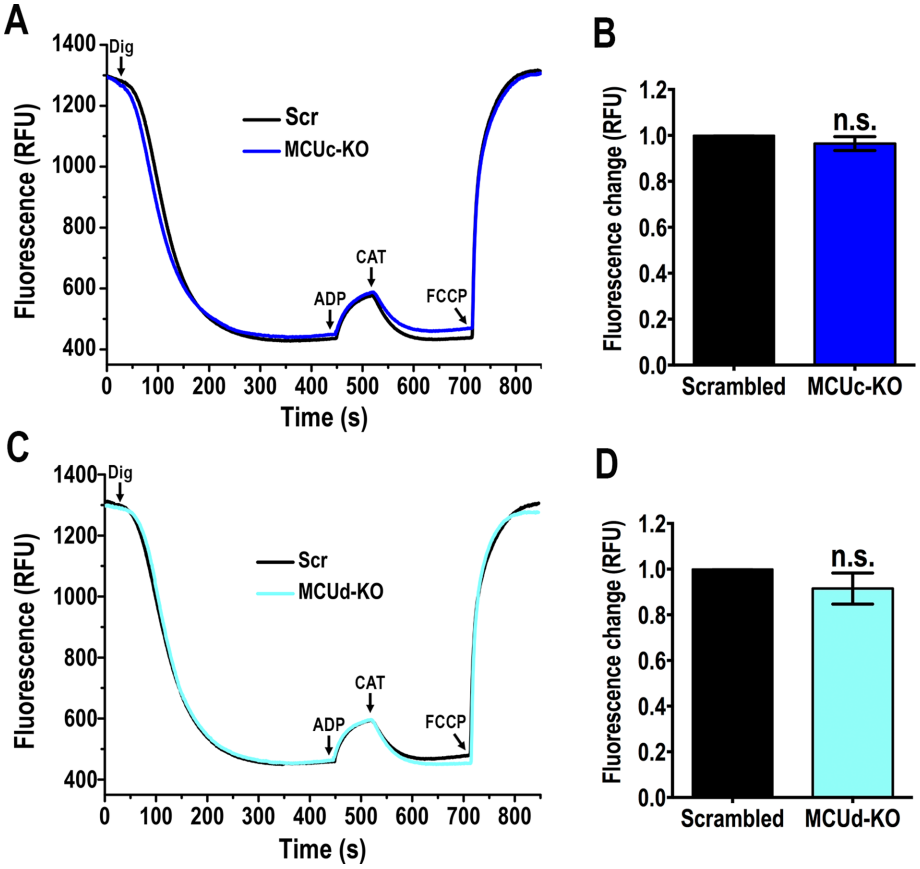

FIGURE 3: Mitochondrial membrane potential in *TcMCUc* and *TcMCUd* KOs. (A) Changes in mitochondrial membrane potential ($\Delta\Psi$m) of DIG-permeabilized epimastigotes as detected by changes in safranine O fluorescence in cells transfected with scrambled sgRNA, Scr, and MCUc-KO, *TcMCUc*-KO cells. The reaction was started with 50 µM DIG, and 250 µM ADP, 1.5 µM CAT, and 4 µM FCCP were added where indicated. (B) Changes in safranine fluorescence after addition of ADP of cells as used in A. (C) Changes in $\Delta\Psi$m of DIG-permeabilized epimastigotes as detected by changes in safranine O fluorescence in cells transfected with scrambled sgRNA (Scr), and MCUd-KO, *TcMCUd*-KO cells. The reaction was started after adding 50 µM DIG using the same experimental conditions and additions as in A. (D) Changes in safranine fluorescence after addition of ADP of cells as used in C. In B and D, values are mean ± SD, $n = 3$, ns, no significant differences (Student's *t* test).

analyses confirmed the expression of these proteins in transfected epimastigotes (Figure 7, A and D). Complementation with a *TcMCUc*^{D157N} or *TcMCUd*^{D141N} mutant, but not with the *TcMCUc*^{E162Q} or *TcMCUd*^{E146Q} mutant, was able to restore mitochondrial Ca^{2+} uptake (Figure 7, B and C, E and F, respectively). As shown above, mitochondria of *TcMCUc*^{E162Q} epimastigotes obtained by in situ mutation were also unable to take up Ca^{2+} (Figure 2, I and J). As occurs with TcMCU and TcMCUb described above, the glutamate residues E162 of TcMCUc and E146 of TcMCUd are essential, whereas the aspartates D157 of TcMCUc and D141 of TcMCUd are important but not essential for Ca^{2+} transport. Interestingly, while in the overexpression experiments, the unprocessed TcMCUc (top band Figure 1A) is weaker, it is the opposite in the complemented *TcMCUc*-KO (Figure 7A). For TcMCUd, the two bands have equivalent intensity in the overexpression experiment (Figure 1A) but the bottom band is relatively more abundant in the complemented cells (Figure 7D). This could suggest that either their processing is different according to the expression level or the differences are due to competition with wild-type (WT) proteins in the overexpression experiment.

In previous work, we reported that human MCU was unable to complement *TcMCU*-KO epimastigotes (Chiurillo *et al.*, 2017). However, it has been reported that human MCU alone is not sufficient to reconstitute Ca^{2+} transport in yeast unless it is expressed together with EMRE (Kovacs-Bogdan *et al.*, 2014). Therefore, we attempted to coexpress HsEMRE with HsMCU in *TcMCU*-KO epimastigotes. Both proteins colocalized to

biotin-labeled fragment of *TcMCUc* (nt +240 to +649). Arrow indicates the expected restriction band recognized by the probe. (E) Schematic representation of the strategy used to generate a *TcMCUd*-KO mutant by CRISPR/Cas9-induced homologous recombination. A double-stranded gDNA break was produced by Cas9 at nt +252 of the *TcMCUd* ORF (660 base pairs). DNA was repaired with a *Bsd* cassette containing 100–base pair homologous regions spanning from nt −100 to +1 and from nt +630 to +730 of the *TcMCUd* locus. (F) Primers (*arrows*) used to verify gene replacement by PCR. The intact locus generates a PCR product of 899 base pairs, while the disrupted locus generates a fragment of 638 base pairs. (G) *TcMCUd* was disrupted at its genomic locus by the *Bsd* gene in the KO cell line. Lanes: 1, 1-kb plus ladder; 2, WT; 3, *TcMCUd*-KO mutant cell line; 4, PCR negative control. (H) Southern blot analysis of WT and *TcMCUd*-KO (KO) epimastigotes. The blot was hybridized with a biotin-labeled probe corresponding to 435 base pairs of *TcMCUd* (nt +1 to +435). Arrow indicates the expected restriction band recognized by the probe. (I) Ca^{2+} uptake by DIG-permeabilized epimastigotes in RFU. Scr, cells transfected with scrambled sgRNA in the absence or presence of 5 µM ruthenium red (+ RR); MCUc-KO, *TcMCUc*-KO cells; MCUc-E162Q, *TcMCUc*-E162Q cells. The reaction was started after adding 50 µM DIG in the presence of 20 µM $CaCl_2$. Where indicated, 4 µM FCCP was added. (J) Quantification of data from three experiments as shown in I. Relative Ca^{2+} uptake at 600 s compared with that of epimastigotes transfected with scrambled control. (K) Ca^{2+} uptake by DIG-permeabilized epimastigotes in RFU. Cells transfected with scrambled sgRNA (Scr) in the absence or presence of 5 µM ruthenium red (+ RR); MCUd-KO, *TcMCUd*-KO cells. The reaction was started after adding 50 µM DIG in the presence of 20 µM $CaCl_2$. Where indicated, 4 µM FCCP was added. (L) Quantification of data from three experiments as shown in K. Relative Ca^{2+} uptake at 600 s compared with that of epimastigotes transfected with scrambled sgRNA. Values in J and L are mean ± SD ($n = 3$); ***$P < 0.001$; one-way ANOVA.

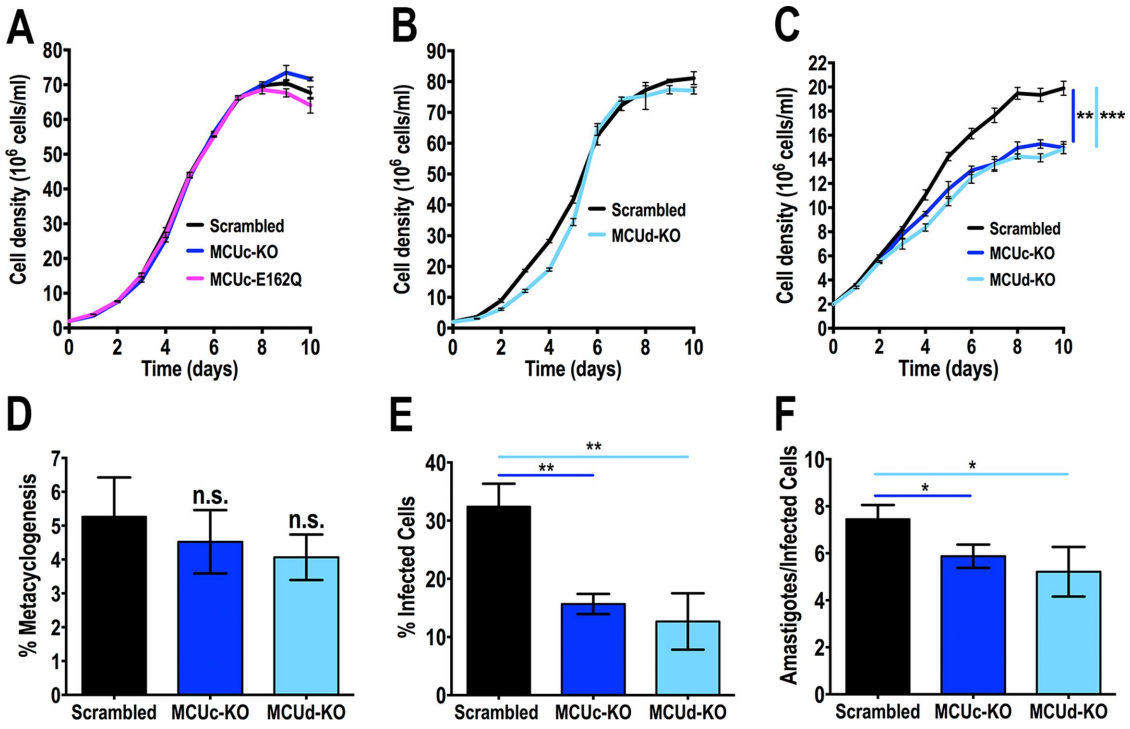

FIGURE 4: Growth, metacyclogenesis, and infectivity of *TcMCUc* and *TcMCUd* KO cells. (A, B) Growth of control (scrambled), *TcMCUc*-KO, and *TcMCUc*-E162Q epimastigotes (A), and control and *TcMCUd*-KO cells in LIT medium (B). No significant differences in growth rates were found using one-way ANOVA with multiple comparisons or Student's *t* test, respectively. (C) Growth of control (scrambled), *TcMCUc*-KO, and *TcMCUd*-KO epimastigotes in low-glucose LIT medium. One-way ANOVA with multiple comparisons was applied to growth rates calculated from each growth curve (**$p < 0.01$, ***$p < 0.001$). (D) Percentage of metacyclic trypomastigotes in epimastigote cultures after incubation in TAU 3AAG medium. Differentiation of epimastigotes to metacyclic trypomastigotes was quantified by staining with DAPI to distinguish the position of the kinetoplast by fluorescence microscopy. Values are mean ± SD (ns, no significant differences) with one-way ANOVA with multiple comparisons. (E, F) *TcMCUc*-KO and *TcMCUd*-KO trypomastigote infection of Vero cells. There were significant differences in the percentage of infected Vero cells at 4 h postinfection (E) as well as in the number of intracellular amastigotes per infected host cell observed 48 h postinfection (F) by both mutant cells. Values are mean ± SD; $n = 3$; *$p < 0.05$, **$p < 0.01$) (one-way ANOVA with Dunnett multiple comparisons).

the mitochondrion of *T. cruzi*, as determined by immunofluorescence analysis (IFA) (Supplemental Figure S6A), and Western blot analyses confirmed the expression of the proteins (Supplemental Figure S6, B C). However, they were unable to reconstitute mitochondrial Ca^{2+} transport in permeabilized epimastigotes (Supplemental Figure S6D). Supplemental Figure S7 shows the complete Western blots.

DISCUSSION

Our studies revealed that *TcMCUc* and *TcMCUd* KO epimastigotes are viable, replicate normally in rich medium, and are able to differentiate into trypomastigotes. However, these mutant cells show a lower growth rate in low-glucose LIT medium, lower rates of respiration, and significantly reduced infectivity and replication inside host cells. In addition, *TcMCUc* and *TcMCUd* KO epimastigotes evidenced an increased capacity to survive an oxidative stress caused by H_2O_2 or a proapoptotic stress caused by C2-ceramide treatment. TcMCUc and TcMCUd, as occurs with TcMCU and TcMCUb (Chiurillo *et al.*, 2017), are essential for mitochondrial Ca^{2+} uptake. Conserved Glu (E) residues in the WDXXEPXXY motif of MCU, MCUb, MCUc and MCUd are critical, while conserved Asp (D) residues are important for Ca^{2+} uptake. The fact that individual ablation of genes encoding each one of the MCU subunits or substitution of critical residues in WDXXEPXXY motif causes suppression of mitochondrial Ca^{2+} uptake suggests that all of them are essential in a putative hetero-oligomeric structure of the *T. cruzi* MCU complex. Each subunit may form part of the oligomer in the same way that several MCU subunits interact in animal and fungal cell mitochondria to form the MCU complex.

The deficient ability of *TcMCUc* and *TcMCUd* KO epimastigotes to grow in low-glucose medium, and of trypomastigotes to infect and to replicate inside host cells as amastigotes, is consistent with their deficient respiratory activity, the more aerobic metabolism of epimastigotes during the stationary phase of growth (Barison *et al.*, 2017), and the relevance on mitochondrial metabolism for the active invasion of host cells by trypomastigotes (Schenkman *et al.*, 1991) and for replication of intracellular amastigotes (Dumoulin and Burleigh, 2018), respectively. As occurs with *TcMCU*-KO epimastigotes, *TcMCUc* and *TcMCUd* KO epimastigotes grow slowly in low-glucose LIT medium, but in contrast to them they have lower respiratory rate suggesting that, as we have found for TcMCUb (Chiurillo *et al.*, 2017), other potential functions of these subunits independent of Ca^{2+} transport are important. It would be interesting to know whether these functions are related to their susceptibility to stress conditions.

Structural studies of the animal (Baradaran *et al.*, 2018) and fungi (Baradaran *et al.*, 2018; Fan *et al.*, 2018; Nguyen *et al.*, 2018; Yoo *et al.*, 2018) recombinant MCU subunit have described the formation of homo-tetramers. The selectivity filter is formed by symmetrical arrangement of WDXXEPXXY sequences in TM2 from each monomer around the pore. The D residues form an acidic mouth with a radius of ~2.2 Å (Site 1), while the E residues form a second acidic ring (Site 2)

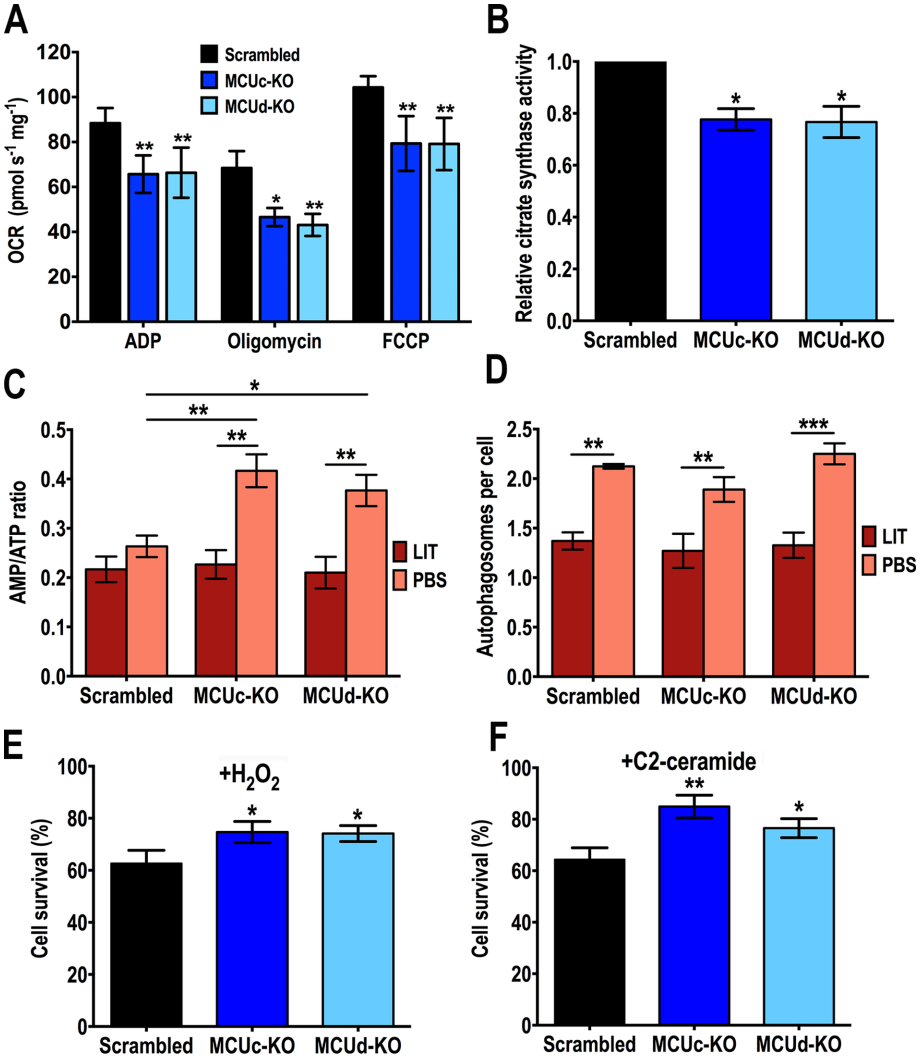

FIGURE 5: Phenotypic changes in *TcMCUc* and *TcMCUd* KO cells. (A) Respiration of *TcMCUc* and *TcMCUd* KO epimastigotes. OCR of DIG-permeabilized control (Scrambled, black bars), *TcMCUc*-KO (dark blue bars), and *TcMCUd*-KO (light blue bars) epimastigotes in the presence of succinate as substrate. Bar charts show OCR after the addition of 100 µM ADP (respiration stimulated by oxidative phosphorylation or OXPHOS), 1 µg/ml oligomycin (minimal respiratory rate), and 1.0 µM FCCP (maximal respiratory capacity). Values are mean ± SD; $n = 3$; $*p < 0.05$, $**p < 0.01$ (two-way ANOVA with Dunnett's multiple comparisons test). (B) Relative citrate synthase activity of control (Scrambled), *TcMCUc*-KO (MCUc-KO), and *TcMCUd*-KO (MCUd-KO) epimastigotes. Values are mean ± SD, $n = 3$, $*p < 0.05$ (one-way ANOVA with multiple comparisons). (C) AMP/ATP ratios of control (Scrambled), *TcMCUc*-KO (MCUc-KO), and *TcMCUd*-KO (MCUd-KO) cells incubated in LIT medium or PBS for 16 h. (D) Number of autophagosomes per cell observed by fluorescence microscopy images of control (Scrambled), *TcMCUc*-KO (MCUc-KO), and *TcMCUd*-KO (MCUd-KO) epimastigotes labeled with anti-TcATG8.1 antibody after incubation in LIT medium or PBS for 16 h. In C and D, values are means ± SD, $n = 3$, $*p < 0.05$, $**p < 0.01$, $***p < 0.001$. Statistical analyses were performed using two-way ANOVA with Sidak's multiple comparisons test. (E, F) Cell viability on apoptotic challenge of control (Scrambled), *TcMCUc*-KO (MCUc-KO), and *TcMCUd*-KO (MCUd-KO) epimastigotes with H_2O_2 (E) and C2-ceramide (F). The results are expressed as the percentage of growth compared with untreated cultures. Values are means ± SD, $n = 3$, $*p < 0.05$, $**p < 0.01$. Statistical analyses were performed using one-way ANOVA with multiple comparisons.

with a pore radius of less than 1 Å (Baradaran *et al.*, 2018). This Site 2 represents the high-affinity binding site for Ca^{2+} in MCU. Accordingly, mutations of the D residues located in the filter region of TcMCU (D223) or TcMCUb (D161), or the D residues located N-terminal to the selectivity filter of TcMCU (D221), TcMCUc (D157), or TcMCUd (D141), reduced but did not completely abolish mitochondrial Ca^{2+} transport.

In contrast, mutations of the E residues of each monomer completely ablated mitochondrial Ca^{2+} transport. Moreover, in a previous work we were able to restore mitochondrial Ca^{2+} uptake in *TcMCU*-KO cells when they were transfected with *TcMCU*$^{R214W/D219V}$ mutant, indicating that these two residues are not important for Ca^{2+} transport in *T. cruzi* (Chiurillo *et al.*, 2017). The residues corresponding to these two residues in other organisms are located in TM1 and the loop region near the WDXXEPXXY motif but outside the channel entrance (Oxenoid *et al.*, 2016; Baradaran *et al.*, 2018; Fan *et al.*, 2018; Nguyen *et al.*, 2018; Yoo *et al.*, 2018). However, the fact that substitutions in the conserved D residues in TcMCU (D221), TcMCUc (D157), and TcMCUd (D141) reduced mitochondrial Ca^{2+} uptake suggests that these D residues located near the WDXXEPXXY motif are important for the function, or even could be part of the selectivity filter of *T. cruzi* MCU.

Our previous work in the related trypanosomatid *T. brucei* (Huang and Docampo, 2018) demonstrated that each of the four MCU monomer subunits interact with each other, as revealed by 1) the formation of large protein complexes detected by blue native gel separation of mitochondrial proteins and labeling with antibodies against all the subunits; and 2) coimmunoprecipitation of the subunits. The strength of their interactions, as evaluated by membrane-based yeast two hybrid assays, suggested the formation of hetero-hexamers (Huang and Docampo, 2018). Deletion of each monomer would affect the formation of the complex and result in loss of mitochondrial Ca^{2+} transport.

Interestingly, the recombinant pore domains of MCU from *Caenorhabditis elegans* (Oxenoid *et al.*, 2016) form homo-pentamers while those from several fungi, like *Neurospora crassa* (Yoo *et al.*, 2018), *Neosartorya fischeri* (Nguyen *et al.*, 2018), *Metarhizium acridum (Fan C, 2018)*, *Fusarium graminearum* (Fan *et al.*, 2018), and *Cyphellophora europea* (Baradaran *et al.*, 2018) and those from zebrafish (Baradaran *et al.*, 2018) form homo-tetramers in vitro. However, which is the oligomeric state in vivo and how animal and fungal MCU interacts with its membrane partners, like MCUb and others in those species, remain to be investigated.

Our attempts to complement *TcMCU*-KO epimastigotes by coexpressing *HsMCU* and *HsEMRE* failed despite their colocalization to the mitochondrion. However, it is possible that the proteins did not insert properly in the inner membrane or with the right topology, failed to interact, or did not form part of the MCU complex.

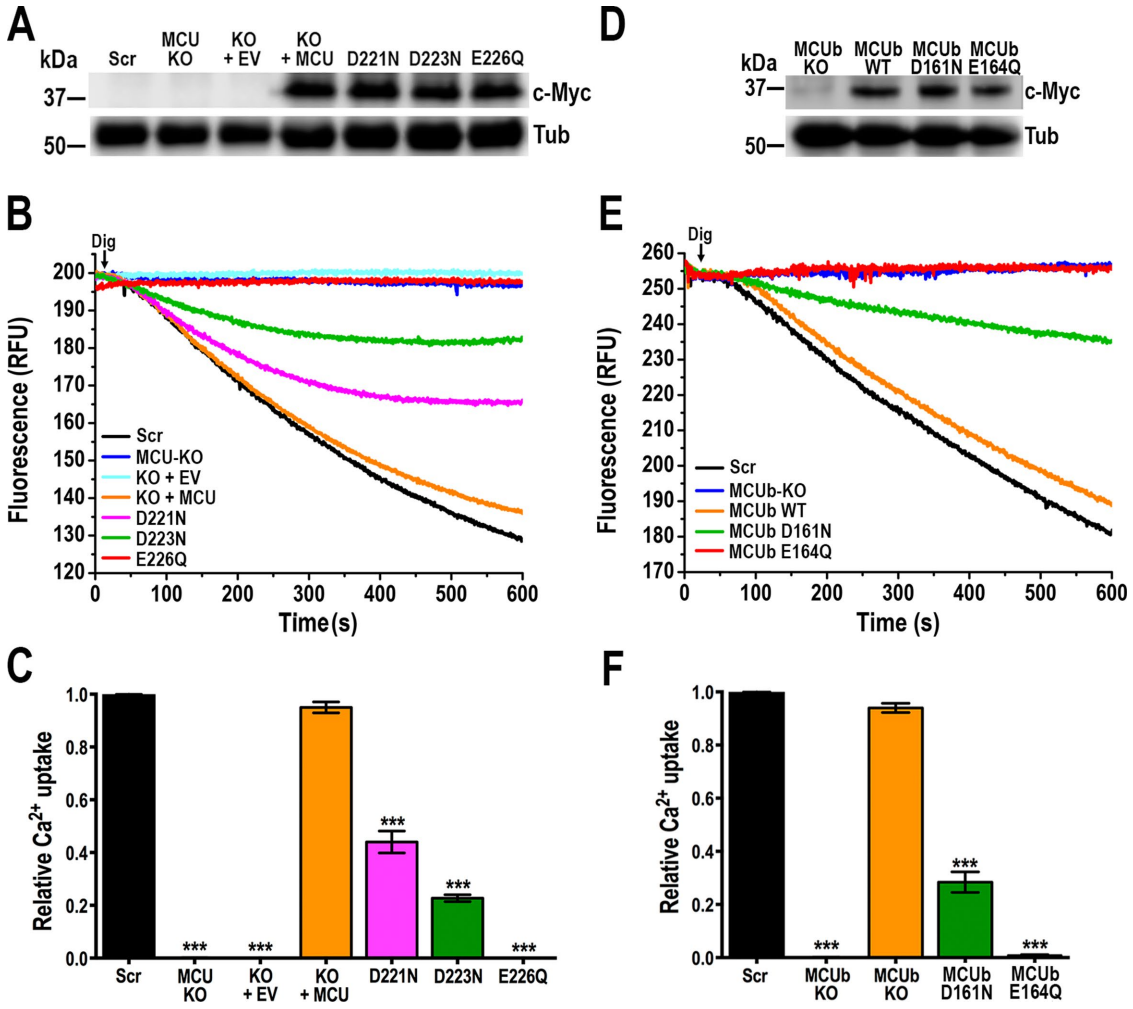

FIGURE 6: Functional mutagenesis of critical amino acid residues at the selectivity filter of *TcMCU* and *TcMCUb*. (A) Western blot analysis of total protein extracts of control (Scr) cells, *TcMCU*-KO (MCU KO), *TcMCU*-KO plus EV (KO + EV), *TcMCU*-KO plus *TcMCU* (KO + MCU), *TcMCU*-KO plus *TcMCU*^{D221N} (D221N), *TcMCU*-KO plus *TcMCU*^{D223N} (D223N), and *TcMCU*-KO plus *TcMCU*^{E226Q} (E226Q) epimastigotes using anti-c-Myc antibodies. Anti-tubulin antibodies (Tub) were used as a loading control. (B) Ca^{2+} uptake reconstitution in DIG-permeabilized epimastigotes. Experimental conditions were as in Figure 1D. (C) Quantification of data from three experiments as shown in B. Relative Ca^{2+} uptake at 500 s compared with controls (Scr). (D) Western blot analysis of total protein extracts of control and knock-in mutated cells, using anti-c-Myc antibodies. Anti-tubulin (Tub) antibodies were used as a loading control. (E) Ca^{2+} uptake in DIG-permeabilized control (Scr), *TcMCUb*-KO (MCUb-KO), and knock-in *TcMCUb*^{control} (MCUb WT), *TcMCUb*^{D161N} (MCUb D161N) and *TcMCUb*^{E164Q} (MCUb E164Q) epimastigotes. Experimental conditions were as in Figure 1D. (F) Quantification of data from three experiments as shown in E. Relative Ca^{2+} uptake at 500 s compared with controls (Scr). Values in C and F are means ± SD ($n = 3$); ***$P < 0.001$; one-way ANOVA.

Interestingly, all *T. cruzi* MCU complex monomers lack the serine amino acid (Ser259 in the human MCU) that has been proposed to be responsible for the sensitivity of the uniporter to the ruthenium red derivative Ru360 (Baughman *et al.*, 2011). In contrast with these structural differences, mitochondrial Ca^{2+} transport in *T. cruzi* is sensitive to Ru360 (unpublished results), suggesting that there is another target for Ru360 besides Ser259.

In conclusion, we demonstrated the Ca^{2+}-conducting activity of all subunits of the *T. cruzi* MCU complex and the involvement of conserved D and E residues in the uniporter function. The two novel subunits present only in trypanosomatids (TcMCUc and TcMCUd), together with the TcMCUb subunit, have Ca^{2+} transport-independent roles and are important for epimastigote growth in low-glucose medium, for trypomastigote infection of host cells, and for intracellular amastigote replication. In addition, we report for the first time a novel CRISPR/Cas9 strategy for doing gene knock-ins in *T. cruzi*.

MATERIALS AND METHODS

Chemicals and reagents

Platinum Taq DNA Polymerase High Fidelity, Calcium Green-5N, MitoTracker Deep Red FM, Alexa–conjugated secondary antibodies, ATP determination kit, Pierce ECL Western blotting substrate, BCA Protein Assay Kit, North2South Biotin Random Prime Labeling Kit, North2South Chemiluminescent Hybridization and Detection Kit, and HA epitope tag monoclonal antibody, and hygromycin B were from Thermo Fisher Scientific. Blasticidin S HCl, BenchMark prestained protein ladder, BenchMark protein ladder,

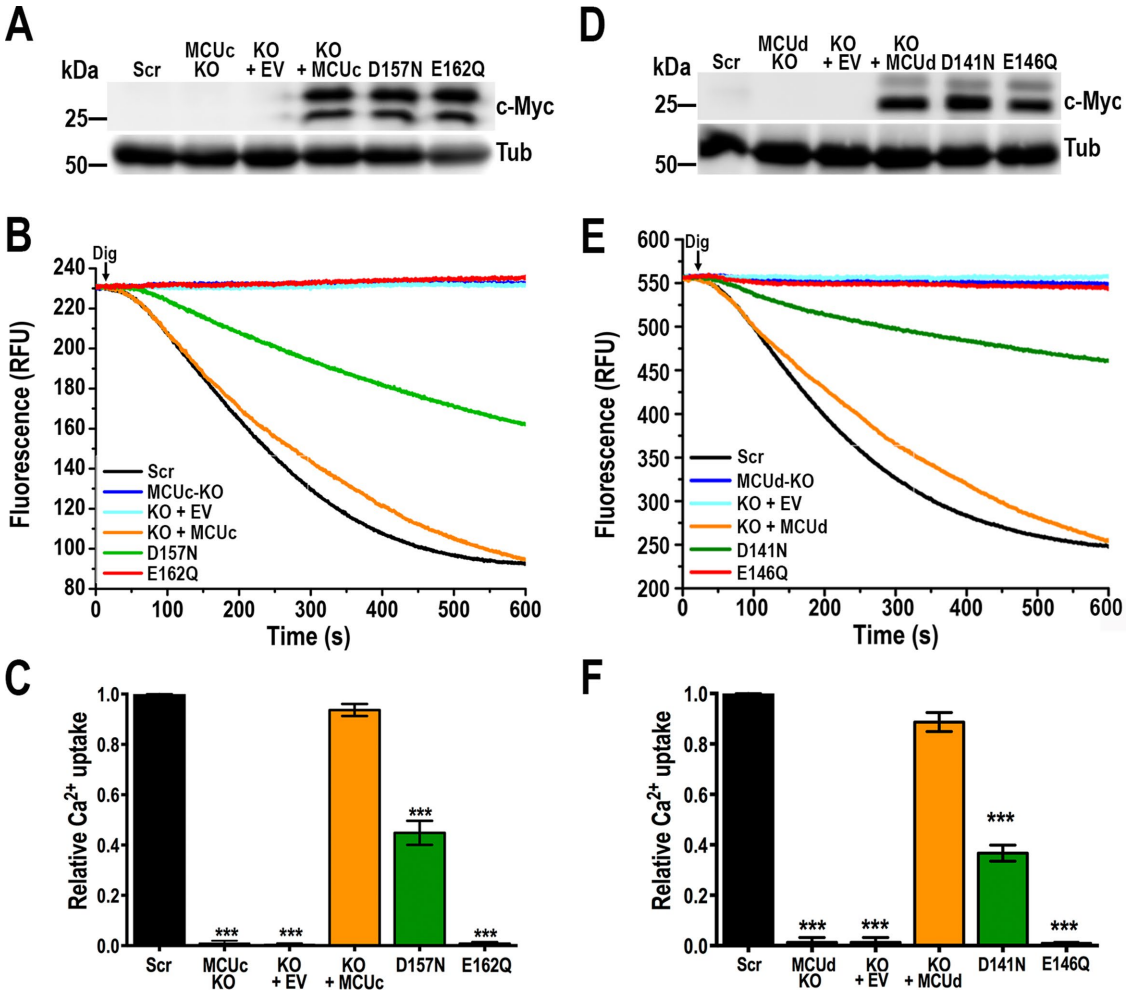

FIGURE 7: Functional mutagenesis of critical amino acid residues at the selectivity filter of *TcMCUc* and *TcMCUd*. (A) Western blot analysis of total protein extracts of control cells (Scr), *TcMCUc*-KO (MCUc KO), *TcMCUc*-KO plus EV (KO + EV), *TcMCUc*-KO plus *TcMCUc* (KO + MCUc), *TcMCUc*-KO plus *TcMCUc*^{D157N} (D157N), and *TcMCUc*-KO plus *TcMCUc*^{E162Q} (E162Q) epimastigotes using anti-c-Myc antibodies. Anti-tubulin (Tub) antibodies were used as a loading control. (B) Ca^{2+} uptake reconstitution in DIG-permeabilized epimastigotes. Experimental conditions were as in Figure 1D. (C) Quantification of data from three experiments as shown in B. Relative Ca^{2+} uptake at 500 s compared with controls (Scr). (D) Western blot analysis of total protein extracts of control cells (Scr), *TcMCUd*-KO (MCUd KO), *TcMCUd*-KO plus EV (KO + EV), *TcMCUd*-KO plus *TcMCUd* (KO + MCUd), *TcMCUd*-KO plus *TcMCUd*^{D141N} (D141N), and *TcMCUd*-KO plus *TcMCUd*^{E146Q} (E146Q) epimastigotes using anti-c-Myc antibodies. Anti-tubulin (Tub) antibodies were used as a loading control. (E) Ca^{2+} uptake reconstitution in DIG-permeabilized epimastigotes. Experimental conditions were as in Figure 1D. (F) Quantification of data from three experiments as shown in E. Relative Ca^{2+} uptake at 500 s compared with controls (Scr). Values in C and F are means ± SD ($n = 3$); ***$P < 0.001$; one-way ANOVA.

Alexa Fluor–conjugated secondary antibodies, and horseradish peroxidase (HRP)-conjugated secondary antibodies were purchased from Life Technologies. Benzonase Nuclease was from Novagen (EMD Millipore, Billerica, MA). Wizard Plus SV Miniprep Purification System, Wizard SV Gel and PCR Clean-Up System, GoTaq DNA Polymerase, and T4 DNA Ligase were from Promega (Madison, WI). Antarctic Phosphatase, restriction enzymes, and Q5 High-Fidelity DNA Polymerase were from New England Biolabs (Ipswich, MA). Fluoromount-G was from SouthernBiotech (Birmingham, AL). Anti-HA High Affinity rat mAb (clone 3F10) was purchased from Roche Applied Science. The pMOTag23M vector (Oberholzer *et al.*, 2006) was from Thomas Seebeck (University of Bern, Bern, Switzerland). DNA oligonucleotides were purchased from Exxtend Biotecnologia (Campinas, Brazil). Precision Plus Protein Dual Color Standards and nitrocellulose membranes were from Bio-Rad. Anti-c-Myc mAb (clone 9E10) was from Santa Cruz Biotechnology (Dallas, TX). Carboxyatractyloside (CAT), oligomycin, safranine O, carbonyl cyanide 4-(trifluoromethoxy) phenylhydrazone (FCCP), Benzonase Nuclease, anti-tubulin mAb, anti-Flag antibody, puromycin, G418, *N*-acetyl-D-sphingosine, mammalian cell protease inhibitor mixture (Sigma P8340), other protease inhibitors, and all other reagents of analytical grade were from Sigma (St. Louis, MO). Rabbit polyclonal antibody against TbVDAC was a gift from Minu Chaudhuri (Meharry Medical College, Nashville, TN). Rabbit polyclonal antibody against TcATG8.1 was a gift from Vanina Alvarez (Universidad Nacional de San Martin, Argentina).

Cell culture

T. cruzi Y strain epimastigotes were cultured in LIT medium containing 10% heat-inactivated fetal bovine serum (FBS) at 28°C

(Bone and Steinert, 1956). CRISPR/Cas9 mutant cell lines were maintained in medium containing 250 µg/ml G418 and 10 µg/ml blasticidin or 5 µg/ml puromycin. When KO cell lines were transfected with constructs made in pTREX-h for complementation experiments, hygromycin B (250 µg/ml) was added to the culture medium. Epimastigotes overexpressing TcMCUc-3xHA or TcMCUd-3xHA were cultured in medium containing 250 g/ml G418. The growth rate of epimastigotes was determined by counting cells in a Muse Cell Analyzer. Tissue culture cell-derived trypomastigotes were obtained from Vero cells infected with metacyclic trypomastigotes obtained as described below. *T. cruzi* trypomastigotes were collected from the culture medium of infected host cells using a modification of the method of Schmatz and Murray (1982) as described previously (Moreno *et al.*, 1994). Vero cells were grown in RPMI supplemented with 10% FBS and maintained at 37°C with 5% CO_2.

TcMCUc and *TcMCUd* overexpression

TcMCUc and *TcMCUd* open reading frames (ORF) (708 and 660 nt, respectively) were PCR amplified using *T. cruzi* Y strain gDNA as template (primers 1, 2, 10, and 11; Supplemental Table S1) and cloned into the pTREX-n/3xHA vector (Chiurillo *et al.*, 2017) by restriction sites *Xba*I/*Xho*I. Gene cloning was confirmed by PCR and sequencing, and constructs were subsequently used to transfect *T. cruzi* epimastigotes. *TcMCUc* and *TcMCUd* overexpression was confirmed by Western blot analysis using anti-HA antibodies.

Knockout of *TcMCUc* and *TcMCUd*

Selection of protospacers was performed using EuPaGDT (Eukaryotic Pathogen CRISPR guide RNA Design Tool, http://grna.ctegd.uga.edu/). The sgRNA sequences to target the *TcMCUc* and *TcMCUd* genes (TryTripDB identifier TcCLB.506181.97 and TcCLB.511367.330, respectively) were amplified by PCR from plasmid pUC_sgRNA using a specific forward primer including the protospacer sequence and a common reverse primer (primers 3, 4, and 12; Supplemental Table S1), as described previously (Lander *et al.*, 2015). PCR-amplified fragments were cloned into Cas9/pTREX-n by the *Bam*HI restriction site (Lander *et al.*, 2015) to generate *TcMCUc*-sgRNA/Cas9/pTREX-n and *TcMCUd*-sgRNA/Cas9/pTREX-n constructs. The sgRNA orientation was verified by PCR using the specific sgRNA forward primers and the HX1 reverse primer (primers 3, 5, and 12; Supplemental Table S1) (Lander *et al.*, 2015) and also by sequencing. A scrambled sgRNA cloned in Cas9/pTREX-n was used as control. DNA donor cassettes designed to promote homologous directed-repair (HDR) and disruption of *TcMCUc* or replacement of *TcMCUd* ORFs were obtained by PCR using a set of 120 nt primers (ultramers). Each one of the ultramers had 20 nt annealing on the Blasticidin-S deaminase (*Bsd*) gene (primers 6, 7, 13, and 14; Supplemental Table S1). Plasmid constructs *TcMCUc*-sgRNA/Cas9/pTREX-n or *TcMCUd*-sgRNA/Cas9/pTREX-n and linear *Bsd* cassette were used to cotransfect *T. cruzi* epimastigotes. After selection with 250 µg/ml G418 and 10 µg/ml blasticidin, *TcMCUc* gene disruption and *TcMCUd* replacement were verified by PCR using primers 8, 9, 15, and 16 (Supplemental Table S1).

Molecular constructs to complement *TcMCU*-KO, *TcMCUc*-KO, and *TcMCUd*-KO mutants

We generated molecular constructs to revert null-mutant phenotypes of *TcMCU*, *TcMCUc*, and *TcMCUd* as well as to investigate critical amino acid residues in the selectivity filter region of the three proteins. We used *TcMCU*-KO epimastigotes that were characterized in a previous work (Chiurillo *et al.*, 2017) and the *TcMCUc*-KO and *TdMCUd*-KO cells obtained in this work. To make the complementation constructs, we followed a two-step-PCR strategy: for *TcMCUc* we used primers that simultaneously eliminate the protospacer adjacent motif (PAM) sequence specific for the sgRNA used to obtain the *TcMCUc*-KO cells and mutate critical residues (Supplemental Table S1; primers 17–20), whereas for *TcMCUd* we first mutated the PAM sequence and then this *TcMCUd*$_{\text{-PAM}}$ sequence was used as a template to introduce the desired mutations in the selectivity filter DNA sequence (Supplemental Table S1; primers 21–26). In the case of *TcMCU*, we used the pTREX-h-*TcMCU*$_{\text{-PAM}}$-HA plasmid as a template (Chiurillo *et al.*, 2017) to introduce mutations by overlap extension PCRs (Supplemental Table S1; primers 27–32). By eliminating the PAM sequence the constitutively expressed Cas9 is not able to target the inserted sequence. We also included a C-terminal 3xc-Myc tag in order to detect the overexpressed protein using the anti-c-Myc antibody. The molecular constructs made were *TcMCU*^{D221N}, *TcMCU*^{D223N}, and *TcMCU*^{E226Q} for *TcMCU*; *TcMCUc*^{D157N} and *TcMCUc*^{E162Q} for *TcMCUc*; and *TcMCUd*^{D141N} and *TcMCUd*^{E146Q} for *TcMCUd* (Supplemental Figure S3). All constructs were made in pTREX-h-3xc-Myc vector (Chiurillo *et al.*, 2017), which confers hygromycin resistance using *Xba*I/*Xho*I restriction sites.

CRISPR/Cas9-induced knock-in mutations in *TcMCUb* and *TcMCUc* genes

To achieve knock-in mutations in critical amino acid residues in the selectivity filter region of *TcMCUb* and *TcMCUc*, we adapted the method developed for CRISPR/Cas9-mediated endogenous C-terminal tagging in *T. cruzi* (Lander *et al.*, 2016). Therefore, we provided donor DNA molecules that by inducing HDR introduce mutations in the genome of parasites and also tag the mutated genes to follow their expression by Western blot and IFA (Supplemental Figure S4). Specific sgRNA targeting the region coding for the selectivity filter of *TcMCUb* was designed and obtained following methodology described above (primer 33; Supplemental Table S1), which in the case of *TcMCUc* was the same designed to disrupt it. To generate donor DNA constructs, we performed a two-step-PCR strategy in which we amplified, in two separate PCRs, a 3′ portion of the gene including a mutated PAM sequence for the specific sgRNA used for the knock-in strategy (primers 34, 35, 42, and 43; Supplemental Table S1), while in the second reaction the 3xc-Myc tag sequence and the puromycin resistance gene were amplified using the pMOTag23M vector as template (primers 36, 37, 44, and 45; Supplemental Table S1) (Oberholzer *et al.*, 2006). Subsequently, we used two 120 nt ultramers in an overlap extension PCR including the two above-mentioned fragments as templates (primers 37, 38, 39, 45, and 46; Supplemental Table S1). Specific forward ultramers including selectivity filters mutations were used to obtain donor DNAs to generate these mutant cells: *TcMCUb*^{D161N} and *TcMCUb*^{E164Q} for *TcMCUb* and *TcMCUc*^{E162Q} for *TcMCUc*. For *TcMCUb*, a forward ultramer with WT sequence was also used to obtain *TcMCUb*^{control} construct. Epimastigotes cotransfected with sgRNA/Cas9/pTREX-n and DNA donor were cultured for 5 wk with G418 and puromycin for selection of double-resistant parasites. Endogenous gene tagging was verified by PCR from gDNA using specific primer sets (primers 9, 40, 41, and 47; Supplemental Table S1) and by Western blot analysis.

Cell transfections

T. cruzi Y strain epimastigotes were transfected as described previously (Chiurillo *et al.*, 2017). Briefly, *T cruzi* epimastigotes in early

exponential phase (4×10^7 cells) were washed with PBS, pH 7.4, at room temperature (RT) and transfected in ice-cold CytoMix (120 mM KCl, 0.15 mM $CaCl_2$, 10 mM K_2HPO_4, 25 mM HEPES, 2 mM EDTA, 5 mM $MgCl_2$, pH 7.6) containing 25 µg of each plasmid construct and 25 µg of donor DNA in 4-mm electroporation cuvettes with three pulses (1500 V, 25 µF) delivered by a Gene Pulser Xcell Electroporation System (Bio-Rad). Transfected epimastigotes were cultured in LIT medium supplemented with 20% heat-inactivated FBS until stable cell lines were obtained. When needed, the antibiotic concentration used for drug selection and maintenance was 250 µg/ml G418, 10 µg/ml blasticidin, 5 µg/ml puromycin, or 250 µg/ml hygromycin. Parasite clones were obtained by limiting dilution.

Southern blot analysis

To confirm gene KOs, 25 µg of gDNA from control (transfected with scramble sgRNA), *TcMCUc*-KO, or *TcMCUd* epimastigotes was digested with *Pst*I enzyme, resolved on a 0.8% agarose gel and restriction fragments were transferred to nylon membranes. PCR-amplified fragments corresponding to 409 and 435 nt of *TcMCUc* and *TcMCUd*, respectively (primers 10, 48, 49, and 50; Supplemental Table S1), were labeled with biotin by random primer method using the North2South Biotin Random Prime Labeling Kit. Hybridization, posthybridization washes, and detection were done with the North2South Chemiluminescent Hybridization and Detection Kit, following manufacturer's recommendations. Signal detection was done using an UVItec Alliance Gel Documentation System (UVItec, Cambridge, UK).

Western blot analysis

Western blots were carried out as described previously (Lander *et al.*, 2010, 2013). Briefly, parasites were harvested and washed twice in PBS and subsequently resuspended in radio-immunoprecipitation assay buffer (150 mM NaCl, 20 mM Tris-HCl, pH 7.5, 1 mM EDTA, 1% SDS, 0.1% Triton X-100) plus a mammalian cell protease inhibitor mixture (diluted 1:250), 1 mM phenylmethylsulfonyl fluoride, 2.5 mM tosyl phenylalanyl chloromethyl ketone, 100 M *N*-(*trans*-epoxysuccinyl)-L-leucine 4-guanidinobutylamide (E64), and Benzonase Nuclease (25 U/ml culture). The cells were then incubated for 1 h on ice, and protein concentration was determined by BCA protein assay. Thirty micrograms of protein from each cell lysate was mixed with 6X Laemmli sample buffer (125 mM Tris-HCl, pH 7, 10% [wt/vol] β-mercaptoethanol, 20% [vol/vol] glycerol, 4.0% [wt/vol] SDS, 4.0% [wt/vol] bromphenol blue) before application to 10% SDS–polyacrylamide gels. Electrophoresed proteins were transferred onto nitrocellulose membranes with a Bio-Rad transblot apparatus. Membranes were blocked with 5% nonfat dried skim milk in PBS-T (PBS containing 0.1% [vol/vol] Tween 20) overnight at 4°C. Next, blots were incubated for 1 h, at RT, with a primary antibody, that is, monoclonal anti-HA (1:5000), monoclonal anti-c-Myc-tag (1:100), and monoclonal anti-tubulin (1:40,000). After three washes with PBS-T, blots were incubated with the secondary antibody (goat anti-mouse immunoglobulin G [IgG] or goat anti-rabbit IgG, HRP-conjugated antibody, diluted 1:10,000). Membranes were washed three times with PBS-T, then blots were incubated with Pierce ECL Plus Substrate, and images were obtained and processed with a C-DiGit Blot Scanner (LI-COR Biosciences).

IFA

Epimastigotes were washed with PBS and fixed with 4% paraformaldehyde in PBS for 1 h at RT. Cells were allowed to adhere to poly-L-lysine–coated coverslips and then permeabilized for 5 min with 0.1% Triton X-100. Permeabilized cells were blocked with PBS containing 3% bovine serum albumin (BSA), 1% fish gelatin, 50 mM NH_4Cl, and 5% goat serum overnight at 4°C. Then, cells were incubated with a primary antibody (monoclonal anti-HA-Tag [1:500], monoclonal anti-c-Myc-tag [1:10], or rabbit polyclonal anti-TbVDAC [1:200]) diluted in 1% BSA in PBS (pH 8.0) for 1 h at RT. Cells were washed three times with 1% BSA in PBS (pH 8.0) and then incubated for 1 h at RT in the dark with Alexa Fluor 488–conjugated goat anti-mouse secondary antibody (1:1000). Then, cells were washed and mounted on slides using Fluoromount-G mounting medium containing 5 µg/ml 4,6-diamidino-2-phenylindole (DAPI) to stain DNA. Controls were done as described above but in the absence of a primary antibody. Differential interference contrast (DIC) and fluorescence optical images were captured with a confocal microscope Leica TCS SP5 II, with a 100× objective (1.44 aperture) under non-saturating conditions that uses photomultiplier tubes for detection of emission, and LAS AF software (Leica, Wetzlar, Germany) for acquisition and processing of digital images.

Metacyclogenesis

Metacyclic trypomastigotes were obtained following the protocol described by Bourguignon *et al.* (1998) with minor modifications. Epimastigotes were obtained after 4 d in LIT medium and incubated for 2 h in triatome artificial urine (TAU) medium (190 mM NaCl, 17 mM KCl, 2 mM $MgCl_2$, 2 mM $CaCl_2$, 0.035% sodium bicarbonate, 8 mM phosphate, pH 6.9, at RT). Then, parasites were incubated for 96 h in TAU 3AAG medium (TAU medium supplemented with 10 mM L-proline, 50 mM sodium L-glutamate, 2 mM sodium L-aspartate, and 10 mM glucose). To increase the number of metacyclic forms to infect Vero cells, the contents of the flask were collected and resuspended in medium containing fresh FBS and incubated at 37°C for 20 h. The complement in fresh FBS kills epimastigotes, whereas metacyclic trypomastigotes survive. Samples were harvested from the TAU 3AAG plus FBS-containing medium at days 5 and 10 of cultivation.

In vitro infection assay

Gamma-irradiated (2000 radiation-absorbed doses) Vero cells (4.5×10^5 cells) were plated onto sterile coverslips in a 12-well plate and incubated overnight at 35°C, 7% CO_2, in RPMI medium plus 10% fresh FBS. Tissue culture-derived trypomastigotes were incubated at 4°C overnight to allow amastigotes to settle from swimming trypomastigotes. Trypomastigotes from the supernatants of these collections were counted and used to infect the coverslips at a 10:1 ratio of parasites to host cells. At 4 h postinfection, coverslips were washed extensively with Hank's balanced salt solution, followed by PBS, pH 7.4, to remove any extracellular parasites. Coverslips were fixed immediately in 4% paraformaldehyde in PBS, pH 7.4, at 4°C for 30 min. Coverslips were washed once with PBS and mounted onto glass slides in Fluoromount-G containing 15 µg/ml DAPI, which stains host and parasite DNA. Coverslips were viewed on an Olympus BX60 microscope to quantify the number of host cells that contained intracellular parasites and the number of intracellular parasites per cell in randomly selected fields. Three hundred host cells were counted per sample in three independent experiments. To quantify amastigote replication, the following modifications were used: host cells were infected at a ratio of 10 parasites to one host cell, and coverslips were allowed to incubate for 48 h postinfection at 35°C, 7% CO_2, prior to fixation and DAPI staining. Coverslips were mounted onto glass slides and analyzed by fluorescence microscopy. Amastigotes in infected cells were counted using a 100× objective.

Cellular respiration

The OCR of DIG-permeabilized epimastigotes was measured using a high-resolution respirometer (Oroboros Oxygraph-2k, Innsbruck, Austria) with DatLab 4 software for data acquisition and analysis, and calibrated as reported by its manufacturer. Cells (1×10^8) were incubated at 28°C in a 2 ml chamber containing 125 mM sucrose, 65 mM KCl, 10 mM HEPES-KOH, pH 7.2, 2.5 mM K_2PO_4, 1 mM $MgCl_2$, 50 µM EGTA, 5 mM succinate, and 25 µM DIG. OCR was calculated as the negative time derivative of oxygen concentration measured in the closed respirometer chambers and expressed per milligram of protein. Data were recorded at 2-s intervals, and 10 data points were used to calculate the slope of the OCR plot through a polynomial fit with DatLab 4 software, as described (Pesta and Gnaiger, 2012).

Citrate synthase activity

Citrate synthase activity was measured using a previously described protocol (Figueira *et al.*, 2011) adapted to trypanosomes (Chiurillo *et al.*, 2017). Briefly, the conversion of oxaloacetate and acetyl-CoA to citrate and SH-CoA was monitored by quantification of the colorimetric product thionitrobenzoic acid (Shepherd and Garland, 1969). *T. cruzi* epimastigotes in early exponential phase (~1×10^8 cells) were washed twice with PBS and incubated in lysis buffer (10 mM Tris-HCl, pH 7.4, 1 mM EDTA, 0.1% Triton X-100, and 25 U of Benzonase Nuclease) for 10 min on ice. Then, proteins were quantified by BCA protein assay and 260-µl reactions were set up in buffer containing 5 µg protein, 250 µM oxaloacetate, 50 µM acetyl-CoA, 100 µM 5,5-dithio-bis(2-nitrobenzoic acid), and 10 mM Tris-HCl, pH 8.0. The increase in absorbance at 412 nm was monitored for 20 min at 28°C using a microplate reader (PowerWave XS 2; BioTek Instruments, Winooski, VT). Values of V_{max} were normalized taking scrambled cell line as reference value.

Mitochondrial membrane potential

Mitochondrial membrane potential was assessed spectrofluorometrically using the indicator dye safranine O, as described previously (Figueira *et al.*, 2012; Chiurillo *et al.*, 2017). Briefly *T cruzi* epimastigotes (5×10^7 cells) were incubated at 28°C in reaction buffer (125 mM sucrose, 65 mM KCl, 10 mM HEPES-KOH buffer, pH 7.2, 1 mM $MgCl_2$, 2.5 mM potassium phosphate; 1.95 ml) containing 5 mM succinate, 0.2% BSA, 50 µM EGTA, and 5 µM safranine O, and the reaction was started with DIG (50 µM). ADP (250 µM), CAT (1.5 µM), and FCCP (4 µM) were added to the media at different time points. Fluorescence changes were monitored on a Hitachi F-7000 spectrofluorometer (excitation at 495 nm and emission at 586 nm).

Mitochondrial calcium transport

The uptake of Ca^{2+} by permeabilized *T. cruzi* epimastigotes was assayed by fluorescence of Calcium Green-5N probe at 28°C, as described previously (Chiurillo *et al.*, 2017). Briefly, cells were collected by centrifugation at 1000 × *g* for 7 min and washed twice with buffer A with glucose (BAG; 116 mM NaCl, 5.4 mM KCl, 0.8 mM $MgSO_4$, 5.5 mM D-glucose, and 50 mM HEPES, pH 7.0). Epimastigotes were resuspended to a final density of 1×10^9 cells/ml in BAG and kept on ice. Before each experiment, a 50-µl aliquot of *T. cruzi* epimastigotes (5×10^7 cells) was added to the reaction buffer (125 mM sucrose, 65 mM KCl, 10 mM HEPES-KOH buffer, pH 7.2, 1 mM $MgCl_2$, 2.5 mM potassium phosphate; 1.95 ml) containing 5 mM succinate, 50 µM EGTA, and 0.5 µM Calcium Green-5N. Ca^{2+} needed to reach 20 µM free Ca^{2+} was added according to the calculation made with software Maxchelator Calculator v1.2 (https://somapp.ucdmc.ucdavis.edu/pharmacology/bers/maxchelator/CaEGTA-NIST.htm). Mitochondrial Ca^{2+} uptake was initiated by the addition of 50 µM DIG. FCCP (4 µM) was added in each experiment when Ca^{2+} uptake reached a steady state level. Fluorescence changes were monitored in the Hitachi F-7000 spectrofluorometer (excitation at 506 nm and emission at 532 nm).

Autophagy assay

Evaluation of autophagy was performed by determining expression of the TcAtg8.1 autophagy marker in *T. cruzi* epimastigotes grown in LIT medium and under starvation conditions (PBS). Autophagosome formation was estimated by immunofluorescence analyses using anti-TcATG8.1 antibody as described (Alvarez *et al.*, 2008). For starvation induction, mid-log parasites were washed twice with PBS, resuspended in the same buffer at a concentration of 5×10^7 cells/ml, and incubated for 16 h at 28°C as described previously (Alvarez *et al.*, 2008).

Measurement of adenine nucleotide levels

Control and mutant epimastigotes were harvested and washed once with Buffer A (116 mM NaCl, 5.4 mM KCl, 0.8 mM $MgSO_4$, and 50 mM HEPES at pH 7.0). After washing, 1×10^8 cells per treatment were centrifuged and resuspended in 100 µl of Buffer A and then lysed on ice for 30 min by the addition of 150 µl of 0.5 M $HClO_4$. The lysates were neutralized (pH 6.5) by the addition of 60 µl of 0.72 M KOH/0.6 M $KHCO_3$. Samples were centrifuged at 1000 × *g* for 5 min and the supernatant was separated for adenine nucleotide determination. ATP, ADP, and AMP in extracted samples were quantified by a luciferin-luciferase bioluminescence assay in a plate reader as described (Huang *et al.*, 2013). Briefly, we used an ATP Determination Kit according to manufacturer's instructions with adenylate kinase and/or nucleoside-diphosphate kinase (NDK) (Sigma). To determine the amount of adenine nucleotides, four measurements were taken of three different reactions for each sample by endpoint determination of the ATP concentration: one reaction without the addition of any ATP-generating enzyme (for ATP), another reaction adding NDK (for ATP + ADP), and the third reaction adding both adenylate kinase and NDK (for ATP + ADP + AMP). The amount of ADP was obtained by subtracting the ATP value from the (ATP + ADP) value, and the amount of AMP was calculated from the difference between the (ATP + ADP + AMP) content and the (ATP + ADP) content.

Survival to H_2O_2 and C2-ceramide

To test the ability of *TcMCUc*-KO and *TcMCUd*-KO parasites to survive to oxidative stress, parasite cultures (2 ml LIT medium + 10% BFS) containing 1×10^7 cells/ml were treated with 0 or 225 mM H_2O_2. After 4 h parasites were diluted 1/5 in 2 ml LIT medium + 10% BFS. The cells were counted after 72 h. The ability of *TcMCUc*-KO and *TcMCUd*-KO cells to survive to the apoptosis inducer C2-ceramide (*N*-acetyl-D-sphingosine) was tested by treating 2×10^6 cells with 100 µM C2-ceramide for 20 h at 28°C. In both experiments, the results were expressed as the percentage of growth compared with untreated cultures. The cell numbers were determined in a cytometer chamber using the trypan blue dye to differentiate living and dead cells. The experiments were performed in triplicate.

Phylogenetic analysis

The phylogenetic tree shown in Supplemental Figure S1 was built with MEGA7 (Kumar *et al.*, 2016) using the Neighbor-Joining method (Saitou and Nei, 1987) and the bootstrap method with 1000 replicates (Felsenstein, 1985). The evolutionary distances were computed using the JTT matrix-based method (Jones *et al.*, 1992).

Statistical analysis

Statistical analyses were performed with GraphPad Prism software (La Jolla, CA), version 6.0. Reported values are means ± SD of *n* biological experiments, as indicated in the figure legends. The level of significance was evaluated by Student's *t* test for comparisons between two cell lines, one-way analysis of variance (ANOVA) for comparisons between more than two cell lines, and two-way ANOVA with multiple comparisons for analyses of grouped data.

ACKNOWLEDGMENTS

We thank Vanina Alvarez (University of San Martin, Argentina) for TcATG8.1 antibodies, Minu Chaudhuri (Meharry University) for the VDAC antibodies, Thomas Seebeck (University of Bern, Bern, Switzerland) for the pMOTag23M vector, Melissa Storey (University of Georgia) for help with the host invasion and replication assays, and the staff of the Life Sciences Core Facility (LaCTAD) from State University of Campinas (UNICAMP) for the acquisition of the confocal microscopy images. This work was funded by the São Paulo Research Foundation (FAPESP), Brazil (2013/50624-0), and the National Institutes of Health (grant AI107663). N.L. and M.A.C. were postdoctoral fellows of FAPESP (grants 2014/08995-4 and 2014/13148-9). M.S.B. was a Master's fellow of FAPESP (grant 2015/25709-8).

REFERENCES

Alvarez VE, Kosec G, Sant'Anna C, Turk V, Cazzulo JJ, Turk B (2008). Autophagy is involved in nutritional stress response and differentiation in *Trypanosoma cruzi*. J Biol Chem 283, 3454–3464.

Baradaran R, Wang C, Siliciano AF, Long SB (2018). Cryo-EM structures of fungal and metazoan mitochondrial calcium uniporters. Nature 559, 580–584.

Barison MJ, Rapado LN, Merino EF, Furusho Pral EM, Mantilla BS, Marchese L, Nowicki C, Silber AM, Cassera MB (2017). Metabolomic profiling reveals a finely tuned, starvation-induced metabolic switch in *Trypanosoma cruzi* epimastigotes. J Biol Chem 292, 8964–8977.

Baughman JM, Perocchi F, Girgis HS, Plovanich M, Belcher-Timme CA, Sancak Y, Bao XR, Strittmatter L, Goldberger O, Bogorad RL, *et al*. (2011). Integrative genomics identifies MCU as an essential component of the mitochondrial calcium uniporter. Nature 476, 341–345.

Bone GJ, Steinert M (1956). Isotopes incorporated in the nucleic acids of *Trypanosoma mega*. Nature 178, 308–309.

Bourguignon SC, de Souza W, Souto-Padron T (1998). Localization of lectin-binding sites on the surface of *Trypanosoma cruzi* grown in chemically defined conditions. Histochem Cell Biol 110, 527–534.

Carafoli E (2010). The fateful encounter of mitochondria with calcium: how did it happen? Biochim Biophys Acta 1797, 595–606.

Carafoli E, Lehninger AL (1971). A survey of the interaction of calcium ions with mitochondria from different tissues and species. Biochem J 122, 681–690.

Cardenas C, Miller RA, Smith I, Bui T, Molgo J, Muller M, Vais H, Cheung KH, Yang J, Parker I, *et al*. (2010). Essential regulation of cell bioenergetics by constitutive $InsP_3$ receptor Ca^{2+} transfer to mitochondria. Cell 142, 270–283.

Chiurillo MA, Lander N, Bertolini MS, Storey M, Vercesi AE, Docampo R (2017). Different roles of mitochondrial calcium uniporter complex subunits in growth and infectivity of *Trypanosoma cruzi*. mBio 8, e00574-17.

Cruz-Bustos T, Potapenko E, Storey M, Docampo R (2018). An intracellular ammonium transporter is necessary for replication, differentiation, and resistance to starvation and osmotic stress in *Trypanosoma cruzi*. mSphere 3, e00377-17.

De Stefani D, Raffaello A, Teardo E, Szabo I, Rizzuto R (2011). A forty-kilodalton protein of the inner membrane is the mitochondrial calcium uniporter. Nature 476, 336–340.

Docampo R, Lukes J (2012). Trypanosomes and the solution to a 50-year mitochondrial calcium mystery. Trends Parasitol 28, 31–37.

Docampo R, Vercesi AE (1989a). Ca^{2+} transport by coupled *Trypanosoma cruzi* mitochondria *in situ*. J Biol Chem 264, 108–111.

Docampo R, Vercesi AE (1989b). Characteristics of Ca^{2+} transport by *Trypanosoma cruzi* mitochondria *in situ*. Arch Biochem Biophys 272, 122–129.

Docampo R, Vercesi AE, Huang G (2014). Mitochondrial calcium transport in trypanosomes. Mol Biochem Parasitol 196, 108–116.

Dumoulin PC, Burleigh BA (2018). Stress-induced proliferation and cell cycle plasticity of intracellular *Trypanosoma cruzi* amastigotes. mBio 9, e00673-18.

Fan C, Fan M, Orlando BJ, Fastman NM, Zhang J, Xu Y, Chambers MG, Xu X, Perry K, Liao M, Feng L (2018). X-ray and cryo-EM structures of the mitochondrial calcium uniporter. Nature 559, 575–579.

Felsenstein J (1985). Confidence limits on phylogenies: an approach using the bootstrap. Evolution 39, 783–791.

Figueira TR, Castilho RF, Saito A, Oliveira HC, Vercesi AE (2011). The higher susceptibility of congenital analbuminemic rats to Ca^{2+}-induced mitochondrial permeability transition is associated with the increased expression of cyclophilin D and nitrosothiol depletion. Mol Genet Metab 104, 521–528.

Figueira TR, Melo DR, Vercesi AE, Castilho RF (2012). Safranine as a fluorescent probe for the evaluation of mitochondrial membrane potential in isolated organelles and permeabilized cells. Methods Mol Biol 810, 103–117.

Huang G, Docampo R (2018). The mitochondrial Ca^{2+} uniporter complex (MCUC) of *Trypanosoma brucei* Is a hetero-oligomer that contains novel subunits essential for Ca^{2+} uptake. mBio 9, e01700-18.

Huang G, Vercesi AE, Docampo R (2013). Essential regulation of cell bioenergetics in *Trypanosoma brucei* by the mitochondrial calcium uniporter. Nat Commun 4, 2865.

Jones DT, Taylor WR, Thornton JM (1992). The rapid generation of mutation data matrices from protein sequences. Comput Appl Biosci 8, 275–282.

Kovacs-Bogdan E, Sancak Y, Kamer KJ, Plovanich M, Jambhekar A, Huber RJ, Myre MA, Blower MD, Mootha VK (2014). Reconstitution of the mitochondrial calcium uniporter in yeast. Proc Natl Acad Sci USA 111, 8985–8990.

Kroemer G, Galluzzi L, Brenner C (2007). Mitochondrial membrane permeabilization in cell death. Physiol Rev 87, 99–163.

Kumar S, Stecher G, Tamura K (2016). MEGA7: molecular evolutionary genetics analysis version 7.0 for bigger datasets. Mol Biol Evol 33, 1870–1874.

Lander N, Bernal C, Diez N, Anez N, Docampo R, Ramirez JL (2010). Localization and developmental regulation of a dispersed gene family 1 protein in *Trypanosoma cruzi*. Infect Immun 78, 231–240.

Lander N, Chiurillo MA, Bertolini MS, Docampo R, Vercesi AE (2018a). The mitochondrial calcium uniporter complex in trypanosomes. Cell Biol Int 42, 656–663.

Lander N, Chiurillo MA, Bertolini MS, Storey M, Vercesi AE, Docampo R (2018b). Calcium-sensitive pyruvate dehydrogenase phosphatase is required for energy metabolism, growth, differentiation, and infectivity of *Trypanosoma cruzi*. J Biol Chem 293, 17402–17417.

Lander N, Li ZH, Niyogi S, Docampo R (2015). CRISPR/Cas9-induced disruption of paraflagellar rod protein 1 and 2 genes in *Trypanosoma cruzi* reveals their role in flagellar attachment. mBio 6, e01012-15.

Lander N, Chiurillo MA, Storey M, Vercesi AE, Docampo R (2016). CRISPR/Cas9-mediated endogenous C-terminal tagging of *Trypanosoma cruzi* genes reveals the acidocalcisome localization of the inositol 1,4,5-trisphosphate receptor. J Biol Chem 291, 25505–25515.

Lander N, Ulrich PN, Docampo R (2013). *Trypanosoma brucei* vacuolar transporter chaperone 4 (TbVtc4) is an acidocalcisome polyphosphate kinase required for in vivo infection. J Biol Chem 288, 34205–34216.

Lisvane Silva P, Mantilla BS, Barison MJ, Wrenger C, Silber AM (2011). The uniqueness of the *Trypanosoma cruzi* mitochondrion: opportunities to identify new drug target for the treatment of Chagas disease. Curr Pharm Des 17, 2074–2099.

Mallilankaraman K, Cardenas C, Doonan PJ, Chandramoorthy HC, Irrinki KM, Golenar T, Csordas G, Madireddi P, Yang J, Muller M, *et al*. (2012). MCUR1 is an essential component of mitochondrial Ca^{2+} uptake that regulates cellular metabolism. Nat Cell Biol 14, 1336–1343.

McCormack JG, Halestrap AP, Denton RM (1990). Role of calcium ions in regulation of mammalian intramitochondrial metabolism. Physiol Rev 70, 391–425.

Menna-Barreto RF, de Castro SL (2014). The double-edged sword in pathogenic trypanosomatids: the pivotal role of mitochondria in oxidative stress and bioenergetics. Biomed Res Int 2014, 614014.

Monzote L, Gille L (2010). Mitochondria as a promising antiparasitic target. Curr Clin Pharmacol 5, 55–60.

Moreno SN, Silva J, Vercesi AE, Docampo R (1994). Cytosolic-free calcium elevation in *Trypanosoma cruzi* is required for cell invasion. J Exp Med 180, 1535–1540.
Nguyen NX, Armache JP, Lee C, Yang Y, Zeng W, Mootha VK, Cheng Y, Bai XC, Jiang Y (2018). Cryo-EM structure of a fungal mitochondrial calcium uniporter. Nature 559, 570–574.
Oberholzer M, Morand S, Kunz S, Seebeck T (2006). A vector series for rapid PCR-mediated C-terminal in situ tagging of *Trypanosoma brucei* genes. Mol Biochem Parasitol 145, 117–120.
Oxenoid K, Dong Y, Cao C, Cui T, Sancak Y, Markhard AL, Grabarek Z, Kong L, Liu Z, Ouyang B, *et al*. (2016). Architecture of the mitochondrial calcium uniporter. Nature 533, 269–273.
Perocchi F, Gohil VM, Girgis HS, Bao XR, McCombs JE, Palmer AE, Mootha VK (2010). MICU1 encodes a mitochondrial EF hand protein required for Ca^{2+} uptake. Nature 467, 291–296.
Pesta D, Gnaiger E (2012). High-resolution respirometry: OXPHOS protocols for human cells and permeabilized fibers from small biopsies of human muscle. Methods Mol Biol 810, 25–58.
Plovanich M, Bogorad RL, Sancak Y, Kamer KJ, Strittmatter L, Li AA, Girgis HS, Kuchimanchi S, De Groot J, Speciner L, *et al*. (2013). MICU2, a paralog of MICU1, resides within the mitochondrial uniporter complex to regulate calcium handling. PLoS One 8, e55785.
Raffaello A, De Stefani D, Sabbadin D, Teardo E, Merli G, Picard A, Checchetto V, Moro S, Szabo I, Rizzuto R (2013). The mitochondrial calcium uniporter is a multimer that can include a dominant-negative pore-forming subunit. EMBO J 32, 2362–2376.
Saitou N, Nei M (1987). The neighbor-joining method: a new method for reconstructing phylogenetic trees. Mol Biol Evol 4, 406–425.
Sancak Y, Markhard AL, Kitami T, Kovacs-Bogdan E, Kamer KJ, Udeshi ND, Carr SA, Chaudhuri D, Clapham DE, Li AA, *et al*. (2013). EMRE is an essential component of the mitochondrial calcium uniporter complex. Science 342, 1379–1382.
Schenkman S, Robbins ES, Nussenzweig V (1991). Attachment of *Trypanosoma cruzi* to mammalian cells requires parasite energy, and invasion can be independent of the target cell cytoskeleton. Infect Immun 59, 645–654.
Schmatz DM, Murray PK (1982). Cultivation of *Trypanosoma cruzi* in irradiated muscle cells: improved synchronization and enhanced trypomastigote production. Parasitology 85, 115–125.
Sen N, Majumder HK (2008). Mitochondrion of protozoan parasite emerges as potent therapeutic target: exciting drugs are on the horizon. Curr Pharm Des 14, 839–846.
Shepherd D, Garland PB (1969). The kinetic properties of citrate synthase from rat liver mitochondria. Biochem J 114, 597–610.
Tomar D, Dong Z, Shanmughapriya S, Koch DA, Thomas T, Hoffman NE, Timbalia SA, Goldman SJ, Breves SL, Corbally DP, *et al*. (2016). MCUR1 is a scaffold factor for the MCU complex function and promotes mitochondrial bioenergetics. Cell Rep 15, 1673–1685.
Urbina JA, Docampo R (2003). Specific chemotherapy of Chagas disease: controversies and advances. Trends Parasitol 19, 495–501.
Vaidya AB (2004). Mitochondrial and plastid functions as antimalarial drug targets. Curr Drug Targets Infect Disord 4, 11–23.
Yoo J, Wu M, Yin Y, Herzik MA Jr, Lander GC, Lee SY (2018). Cryo-EM structure of a mitochondrial calcium uniporter. Science 361, 506–511.